A 50-kW Three-Phase Wireless Power Transfer System Using Bipolar Windings and Series Resonant Networks for Rotating Magnetic Fields

Jason Pries, *Member, IEEE*, Veda Prakash Nagabhushana Galigekere, *Senior Member, IEEE*, Omer C. Onar, *Senior Member, IEEE*, and Gui-Jia Su, *Senior Member, IEEE*

***Abstract*—The mass and volume of wireless power transfer (WPT) systems for charging electric vehicles are directly related to the rated power of the system. The difficulties of high-power wireless charging are exacerbated by the need to meet the same practical constraints associated with vehicle integration as lower power systems. Therefore, more advanced techniques are necessary to improve power density and specific power of wireless charging systems for high-power applications. This article presents theory and analysis of three-phase inductive WPT systems with bipolar phase windings. Magnetic coupler topologies and the theoretical and practical aspects of series three-phase resonant compensation networks are discussed. The systems under consideration are designed to utilize rotating magnetic fields to achieve a power transfer characteristic that is temporally smoother than single-phase systems. Other benefits associated with rotating magnetic field based WPT, including reduced ferrite mass, filter component requirements, and electromagnetic field emissions, are discussed. Experimental results of a prototype system are presented in both aligned and misaligned configurations. The system is demonstrated transferring 50 kW with 95% dc-to-dc efficiency over a 150-mm airgap in the aligned case. On a per-pad basis, the magnetic couplers achieve a power density of 195 kW/m^2 and a specific power of 3.65 kW/kg. This article is accompanied by a video of the rotating magnetic field produced by a simulated three-phase WPT system.**

***Index Terms*—Electric vehicles (EVs), inductive charging, resonance, three-phase electric power, tuned circuits, wireless charging, wireless power transfer (WPT).**

Manuscript received May 6, 2019; revised July 30, 2019; accepted September 5, 2019. Date of publication October 9, 2019; date of current version February 11, 2020. This manuscript has been authored by UT-Battelle, LLC, under contract DE-AC05-00OR22725 with the US Department of Energy (DOE). The US government retains and the publisher, by accepting the article for publication, acknowledges that the US government retains a nonexclusive, paid-up, irrevocable, worldwide license to publish or reproduce the published form of this manuscript, or allow others to do so, for US government purposes. DOE will provide public access to these results of federally sponsored research in accordance with the DOE Public Access Plan (https://energy.gov/downloads/doepublic-access-plan). Recommended for publication by Associate Editor O. Lucia. *(Corresponding author: Jason Pries.)*

The authors are with the Power Electronics and Electric Machinery Research Group, Electrical and Electronic Systems Research Division, Oak Ridge National Laboratory, Oak Ridge TN 37830 USA (e-mail: jason.pries@ieee.org; galigekerevn@ornl.gov; onaroc@ornl.gov; sugj@ornl.gov).

This article has supplementary downloadable material available at http://ieeexplore.ieee.org, provided by the authors.

Color versions of one or more of the figures in this article are available online at http://ieeexplore.ieee.org.

Digital Object Identifier 10.1109/TPEL.2019.2942065

I. Introduction

THE U.S. Department of Energy recently performed a technology gap assessment analyzing the technical barriers preventing electric vehicle (EV) recharging powers from reaching 400 kW [1]. This rate is projected to provide parity between EV and traditional vehicle refueling times. High-power wireless power transfer (WPT) is an attractive option for fast charging because the user is not required to handle any high-power equipment. WPT is also a key enabling technology for autonomous vehicles. However, power transfer capability of WPT systems is closely linked to the size and mass of the transmitter and receiver pads. The feasibility of high-power WPT greatly depends on the ability to improve the power density and specific power of wireless charging systems.

Most WPT systems investigated in the literature are the single-phase type [2], [3]. However, as WPT systems increase in power, design constraints imposed by safety considerations become more challenging to satisfy. Polyphase systems can achieve higher power transfer capabilities given electromagnetic field emissions and foreign object heating (touch safety) limits. This is because polyphase systems can achieve a more uniform magnetic field distribution, allowing better utilization of the allocated space. Numerous three-phase WPT systems have been investigated in the literature; they vary greatly in form and function depending on the particular application area. These systems are typically differentiated by magnetic coupler topologies and power electronics.

Most of the research associated with three-phase WPT systems has been performed in the context of dynamic EV charging systems [4]–[18]. Some researchers have investigated three-phase coupler topologies suitable for stationary charging of EVs using unipolar phase windings [19]–[26]. Others have developed three-phase WPT systems optimized for particular applications such as unmanned vehicles [27]–[30], contactless slipring systems [31], [32], and omnidirectional systems to cope with arbitrary receiver alignment [33]–[36]. Multiple orthogonal coil structures have been analyzed using the direct–quadrature–zero transformation to provide six degrees of freedom charging capability to Internet of Things devices using rotating magnetic fields [37], [38].

Nonzero interphase mutual inductance has been identified as a problem in three-phase WPT systems. When the interphase

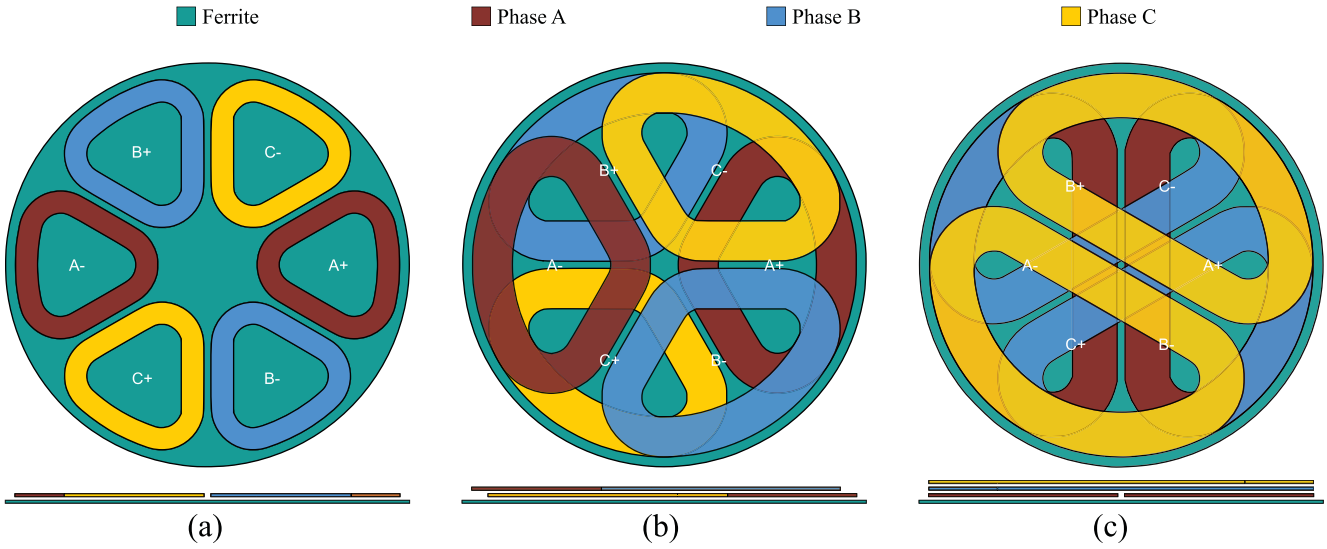

Fig. 1. Bipolar three-phase WPT coil system topologies. (a) Single layer with coil span of 60°. (b) Double layer with coil span of 120°. (c) Triple layer with coil span of 180°. The single-layer coil can achieve balanced inductances when the positive and negative poles are connected in series. Both the single- and double-layer coils can achieve balanced phase inductances when the positive and negative poles are connected in series. The double-layer coil has unbalanced inductances when the poles are connected in parallel since the top and bottom layers are different distances from the backing ferrite. The triple-layer coil is an unbalanced system for the same reason.

mutual inductance is not accounted for in the resonant compensation network, power transfer capability is compromised [25], [26]. Some researchers have demonstrated it is possible to adjust for the impact of the interphase mutual inductance in their systems [16]–[20], [28], [39], [40]. An alternative approach is to design the three-phase pads in such a way to eliminate the interphase mutual inductance, allowing independent excitation of the phases and improved misalignment efficiency [21], [22].

Even when the interphase mutual inductance is accounted for in balanced systems, unbalanced inductances still present a problem. One study of three-phase track systems found that the resonant network tuning must be modified to compensate for unbalanced interphase mutual inductances [5]. One approach included additional ferrite cores between the phases to improve the current balance [6]. Other research derived tuning capacitor equations for series-compensated wye-connected three-phase resonant networks, which considered general unbalanced interphase mutual inductances [39], [40].

This article extends previous work on three-phase WPT systems in several directions to improve power density and specific power of WPT couplers. Planar bipolar three-phase coil topologies for static WPT are discussed. These couplers are designed to utilize the field-shaping nature of the bipolar phase windings to increase power transfer capability when designed to meet constraints imposed by safety standards. Resonant networks must be tuned properly considering interphase mutual inductances. To this end, a methodology is presented for tuning three-phase resonant networks based on the Clarke transformation, generalizing previous results for three-phase systems with both balanced and unbalanced interphase mutual inductances and nonorthogonal coil structures. Using this methodology, tuning capacitor expressions are derived for four three-phase series resonant networks, two of which have not been previously analyzed in the literature. A prototype of the most promising coupler topology and two resonant networks are tested in both aligned and misaligned conditions.

This article is structured as follows. Section II presents three different bipolar three-phase WPT coil system topologies along with an introduction to their operational theory. Section III develops a general statement of resonance conditions for polyphase systems. Section IV presents a tuning methodology for series-compensated three-phase resonant networks based on the Clarke transformation. Section V compares several coupler topologies designed to maximize power under magnetic field emissions constraints in order to quantify the benefits of three-phase topologies. Section VI presents details of a prototype system. The corresponding experimental results appear in Section VII. Finally, Section VIII provides concluding remarks.

II. Bipolar Three-Phase Coupler Topologies

Three bipolar three-phase coil systems are represented schematically in Fig. 1. Topologically, all the couplers are constructed of three winding pairs. The individual windings composing each pair are wound opposite in polarity. The sense of the winding direction is indicated by a $+$ or $-$. The systems are bipolar in the sense that the flux produced by one coil has a natural return path through its twin. For example, if the current direction through phase A$+$ produces a flux in the positive z-direction, then the current direction through phase A$-$ produces a flux in the negative z-direction.

Structurally, the coil systems differ in two respects: coil pitch and number of layers. If the number of layers is n_l, then the coil pitch must be less than $n_l 60°$. Therefore, the maximum coil pitch for one-, two-, and three-layer coil systems is 60°, 120°, and 180°, respectively. Because each layer is a different distance from the backing ferrite, windings on different layers will have

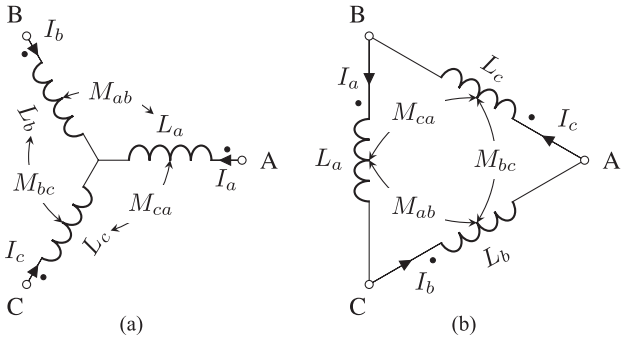

Fig. 2. Circuit diagram of three magnetically coupled inductors. (a) Wye connection. (b) Delta connection.

different self-inductances. Similarly, the mutual inductance between any two phase windings will depend on the layer of each pair.

Consider the single-layer system depicted in Fig. 1(a). Because all of the windings are on the same layer, all individuals will have the same self-inductance, and all pairs will have the same mutual inductance. In the double-layer system in Fig. 1(b), the windings on layer 1 will have one set of self- and mutual inductances, and the windings on layer 2 will have a different set of self- and mutual inductances. However, the positive and negative poles of each phase occur on different layers. Therefore, when the individual phase windings in the double-layer system are connected in series, the overall system has balanced inductances. In the triple-layer system of Fig. 1(c), each layer contains a unique phase. Therefore, this system has naturally unbalanced inductances.

A. Three-Phase Coupled Inductors

The coil systems in Fig. 1 may be modeled as mutually coupled three-phase inductors. Circuit diagrams for wye- and delta-connected coupled inductors are shown in Fig. 2(a) and (b), respectively. The inductances can be compactly represented by a three-phase inductance matrix $\underline{\mathbf{L}}$ given by

$$\underline{\mathbf{L}} = \begin{bmatrix} L_a & M_{ab} & M_{ca} \\ M_{ab} & L_b & M_{bc} \\ M_{ca} & M_{bc} & L_c \end{bmatrix}. \tag{1}$$

Because of the reciprocal nature of magnetic flux coupling between two coils, $\underline{\mathbf{L}}$ is symmetric. The matrix is uniquely defined by three self-inductances (L_a, L_b, L_c) and three mutual inductances (M_{ab}, M_{bc}, M_{ca}). Unless otherwise noted, unbalanced inductances ($L_a \neq L_b \neq L_c$ and $M_{ab} \neq M_{bc} \neq M_{ca}$) are assumed. The mutual inductances are signed.

Given a frequency $\omega = 2\pi/T$ with period T, the impedance matrix associated with the inductance matrix is $\underline{\mathbf{Z}}_L = j\omega\underline{\mathbf{L}}$. The complex valued inductor phase currents are given by the current vector $\mathbf{I}_L = [I_a \quad I_b \quad I_c]$. In the wye-connected configuration, the line currents are equal to the phase currents. In the delta-connected configuration, the line currents are equal to the difference of the phase currents connected to the corresponding line node. Mathematically, the line currents $\mathbf{I}_l = [I_A \quad I_B \quad I_C]^T$ can be written as

$$\mathbf{I}_l = \begin{cases} \mathbf{I}_L & \text{wye connection} \\ \underline{\mathbf{D}}_\Delta \mathbf{I}_L & \text{delta connection.} \end{cases} \tag{2}$$

In (2), $\underline{\mathbf{D}}_\Delta$ is a matrix taking the difference between adjacent phase currents given by

$$\underline{\mathbf{D}}_\Delta = \begin{bmatrix} 0 & -1 & 1 \\ 1 & 0 & -1 \\ -1 & 1 & 0 \end{bmatrix}. \tag{3}$$

The phase voltages associated with the coupled inductor systems are given by $\mathbf{V}_L = \mathbf{Z}_L\mathbf{I}_L$. In the delta-connected configuration, the line-to-line voltages are equal to the phase voltages. In the wye-connected configuration, the line-to-line voltages are equal to the difference of the phase voltages connected between the corresponding line nodes. Mathematically, the line-to-line voltages $\mathbf{V}_{ll} = [V_{AB} \quad V_{BC} \quad V_{CA}$ can be written as

$$\mathbf{V}_{ll} = \begin{cases} \underline{\mathbf{D}}_Y \mathbf{V}_L & \text{wye connection} \\ \underline{\mathbf{P}}\mathbf{V}_L & \text{delta connection.} \end{cases} \tag{4}$$

In (4), $\underline{\mathbf{D}}_Y$ is a matrix taking the difference between adjacent phase voltages given by

$$\underline{\mathbf{D}}_Y = \begin{bmatrix} 1 & -1 & 0 \\ 0 & 1 & -1 \\ -1 & 0 & 1 \end{bmatrix}. \tag{5}$$

The permutation matrix given by $\underline{\mathbf{P}}$ is

$$\underline{\mathbf{P}} = \begin{bmatrix} 0 & 0 & 1 \\ 1 & 0 & 0 \\ 0 & 1 & 0 \end{bmatrix}. \tag{6}$$

A permutation matrix is necessary because, for example, the phase A inductor in Fig. 2(b) appears across the BC terminals.[1]

B. Three-Phase WPT Systems

When two couplers are brought together—one ground assembly (GA) and one vehicle assembly (VA)—the resulting WPT system has a total of six coils. The system can be described by a 6×6 inductance matrix

$$\underline{\mathbf{L}}_{gv} = \begin{bmatrix} \underline{\mathbf{L}}_{gg} & \underline{\mathbf{M}}_{vg} \\ \underline{\mathbf{M}}_{gv} & \underline{\mathbf{L}}_{vv} \end{bmatrix} \tag{7}$$

and an associated 6×1 current vector

$$\mathbf{I}_{L,gv} = \begin{bmatrix} \mathbf{I}_{L,g}^T & \mathbf{I}_{L,v}^T \end{bmatrix}^T. \tag{8}$$

The vectors $\mathbf{I}_{L,g}$ and $\mathbf{I}_{L,v}$ represent the GA and VA phase currents, respectively. The inductance matrices $\underline{\mathbf{L}}_{gg}$ and $\underline{\mathbf{L}}_{vv}$

[1]This may seem a curious convention, but it yields pleasantly symmetric notational results for the tuning capacitor equations in Section IV-B.

represent the self-inductances of the GA and VA as (1). The mutual inductance matrices $\underline{\mathbf{M}}_{vg}$ and $\underline{\mathbf{M}}_{gv}$ represent the magnetic coupling between the GA and VA where

$$\underline{\mathbf{M}}_{gv} = \begin{bmatrix} M_{ga}^{va} & M_{gb}^{va} & M_{gc}^{va} \\ M_{ga}^{vb} & M_{gb}^{vb} & M_{gc}^{vb} \\ M_{ga}^{vc} & M_{gb}^{vc} & M_{gc}^{vc} \end{bmatrix}. \tag{9}$$

The coupling between the GA and VA is symmetric. Therefore, the full inductance matrix associated with the six-coil WPT system is symmetric; $\underline{\mathbf{L}}_{gv} = \underline{\mathbf{L}}_{gv}^T$. While it is true that $\underline{\mathbf{M}}_{gv} = \underline{\mathbf{M}}_{vg}^T$, these matrices are not necessarily self-symmetric. Generally, $\underline{\mathbf{M}}_{gv} \neq \underline{\mathbf{M}}_{gv}^T$ and $\underline{\mathbf{M}}_{vg} \neq \underline{\mathbf{M}}_{vg}^T$ except in special circumstances. Ideally, the power transfer rate will be independent of relative rotations between the GA and VA. If this is the case, $\underline{\mathbf{M}}_{gv}$ should have a circulant structure given by

$$\underline{\mathbf{M}}_{gv}^{\circ} = M_{gv} \begin{bmatrix} \cos(\theta) & \cos\left(\theta - \frac{2\pi}{3}\right) & \cos\left(\theta + \frac{2\pi}{3}\right) \\ \cos\left(\theta + \frac{2\pi}{3}\right) & \cos(\theta) & \cos\left(\theta - \frac{2\pi}{3}\right) \\ \cos\left(\theta - \frac{2\pi}{3}\right) & \cos\left(\theta + \frac{2\pi}{3}\right) & \cos(\theta) \end{bmatrix}. \tag{10}$$

The scalar M_{gv} is the maximum mutual inductance between any two phases and θ is the angle between the GA and VA.

C. Three-Phase Power Expressions

The power transfer of a three-phase WPT system can be expressed either in terms of the coil currents or coil voltages. Given vectors of GA and VA coil currents, the complex power transferred from the GA to the VA is given by

$$P = \begin{cases} +j\omega \mathbf{I}_v^H \underline{\mathbf{M}}_{gv} \mathbf{I}_g \\ -j\omega \mathbf{V}_g^H \underline{\mathbf{M}}_{gv}^{-1} \mathbf{V}_v \end{cases} \tag{11}$$

where $\mathbf{I}_v$ and $\mathbf{I}_g$ are vectors of complex RMS phase currents and $\mathbf{V}_v$ and $\mathbf{V}_g$ are vectors of induced voltages resulting from coupling between the GA and VA. The second expression is derived from the first by noting that $\mathbf{V}_v = j\omega \underline{\mathbf{M}}_{gv} \mathbf{I}_g$ and $\mathbf{V}_g = j\omega \underline{\mathbf{M}}_{gv}^T \mathbf{I}_v$.

Assuming $\underline{\mathbf{M}}_{gv}$ is circulant and that the GA and VA currents have a phase difference equal to $\pi/2 + \theta$, then the current oriented power expression in (11) simplifies to

$$P = \frac{9}{2} \omega M_{gv} I_v I_g \tag{12}$$

where I_g and I_v are the balanced GA and VA rms phase current amplitudes, respectively.

For Y-connected coils, the amplitude of the compensated phase voltages is given by the fundamental harmonic of the line-to-neutral voltage of the inverter phases, which is equal to $2/\pi \cdot V_{\text{dc}}$ under balanced operation. For Δ-connected coils, the amplitude of the compensated phase voltages is given by the fundamental harmonic of the line-to-line voltage of the inverter output, which is equal to $\sqrt{12}/\pi \cdot V_{\text{dc}}$. Assuming the inverter and rectifier voltages are balanced and have a phase difference of $\pi/2 + \theta$, the voltage oriented power expression in (11) simplifies to

$$P = \begin{cases} \frac{4}{\pi^2} \frac{V_{\text{dc},g} V_{\text{dc},v}}{\omega M_{gv}} & \text{Y-connected coils} \\ \frac{12}{\pi^2} \frac{V_{\text{dc},g} V_{\text{dc},v}}{\omega M_{gv}} & \Delta\text{-connected coils} \end{cases} \tag{13}$$

for series compensated systems.

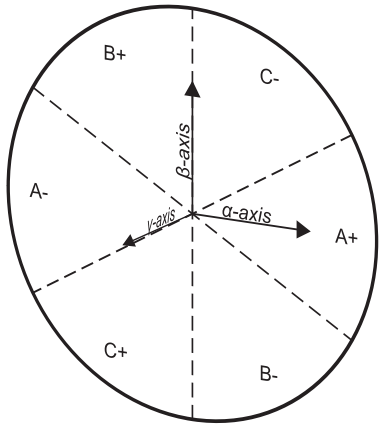

Fig. 3. Definition of the α, β, and γ axes in relationship to the phase winding placement. The α-axis is aligned with phase A; the β-axis is aligned with the midpoint between phases B and C; the γ-axis is orthogonal to the other two, pointing out of the coil plane.

D. Clarke Transformation

The topologies in Fig. 1 are systems with three independent variables that effectively exist in a two-dimensional (2-D) space. An improved understanding and simplified description of three-phase WPT systems can be obtained by transforming the equations into an orthogonal coordinate system. This can be done using the Clarke transformation, which is widely used in the analysis of power systems.

The unitary $\alpha\beta\gamma$ transformation is given by the following matrix:

$$\mathbf{T} = \sqrt{\frac{2}{3}} \begin{bmatrix} 1 & -1/2 & -1/2 \\ 0 & \sqrt{3}/2 & -\sqrt{3}/2 \\ \sqrt{2}/2 & \sqrt{2}/2 & \sqrt{2}/2 \end{bmatrix}. \tag{14}$$

The matrix defining this version of the transformation is orthogonal, that is, its transpose is equal to its inverse

$$\underline{\mathbf{T}}^T \underline{\mathbf{T}} = \underline{\mathbf{I}}. \tag{15}$$

Note that the first two rows of $\underline{\mathbf{T}}$ are samples of the vector $\begin{bmatrix} \cos(\varphi) & \cos(\varphi - 2\pi/3) & \cos(\varphi + 2\pi/3) \end{bmatrix}$ for $\varphi = 0^\circ$ and $\varphi = 90^\circ$. The relationship between the placement of phases A, B, and C and the $\alpha\beta\gamma$ coordinate system is depicted in Fig. 3. The α-axis is aligned with the A+ winding. The β-axis is aligned at the midpoint between the B+ and C− winding. Conceptually, the γ-axis—which represents the zero sequence—is oriented out of the plane of the page.

The vector of phase currents $\mathbf{I}_L^{abc}$ is projected onto the $\alpha\beta\gamma$ coordinate systems through multiplication by $\underline{\mathbf{T}}$

$$\mathbf{I}_L^{\alpha\beta\gamma} = \underline{\mathbf{T}} \mathbf{I}_L^{abc} = \begin{bmatrix} I_\alpha & I_\beta & I_\gamma \end{bmatrix}^T. \tag{16}$$

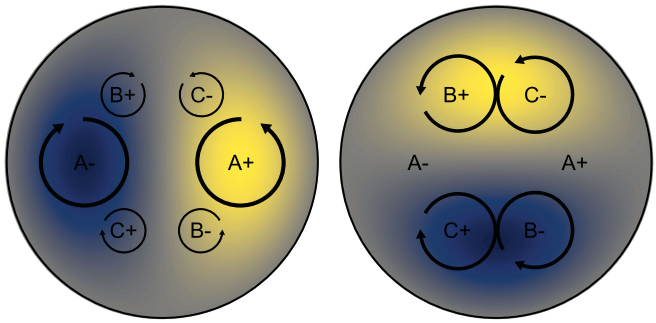

Fig. 4. Schematic representation of (a) α and (b) β modes. The arrows represent the direction of the in-plane phase electrical currents and the colors represent the magnitude and direction of the magnetic flux density out of the plane of the page.

When a distinction must be made, superscripts abc and $\alpha\beta\gamma$ are used to clarify the reference frame in which the variables are expressed. Similarly, the inductance matrix $\underline{\mathbf{L}}^{abc}$ is mapped into the $\alpha\beta\gamma$ reference frame using a similarity transformation

$$\underline{\mathbf{L}}^{\alpha\beta\gamma} = \underline{\mathbf{T}}\underline{\mathbf{L}}^{abc}\underline{\mathbf{T}}^{T} = \begin{bmatrix} L_\alpha & M_{\alpha\beta} & M_{\gamma\alpha} \\ M_{\alpha\beta} & L_\beta & M_{\beta\gamma} \\ M_{\gamma\alpha} & M_{\beta\gamma} & L_\gamma \end{bmatrix}. \tag{17}$$

Generally, all of the 3×1 vectors and 3×3 matrices appearing in this article are transformed the same way.

The result of exciting a bipolar three-phase coil system by pure α and β currents is depicted schematically in Fig. 4. The α mode produces a bipolar flux density distribution primarily aligned with the phase A coils. The β mode produces a bipolar flux density, which is rotated by 90° relative to the α-axis.

Finite-element simulations of single-, double-, and triple-layer coil topologies are shown in Fig. 5. Compared to the approximation in Fig. 4, the spatial flux density distribution in more realistic systems is significantly complicated by the discrete nature of the phase winding layouts. However, the general interpretation of the modes is similar.

Finally, consider the case where α and β modes are excited in quadrature, that is, let $I_\alpha = I$, $I_\beta = jI$, and $I_\gamma = 0$. In the time domain, the current vector is aligned with the α-axis at time $t = 0$. At time $t = T/4$, the current vector is aligned with the β-axis. At intermediate times, the current vector is some linear combination of α and β modes. The excitation of these modes in quadrature results in a rotating current vector that produces a rotating magnetic field.

E. Three-Phase Alternatives

1) Two-Phase Systems: Two-phase couplers may also be used to create a rotating magnetic field. From a power electronics perspective, the system architecture and control can be simplified by using two orthogonal direct and quadrature windings. From a coupler design point of view, it is more difficult to construct a two-layer bipolar two-phase system with balanced inductances because each pole of each phase must occupy half of the top layer and half of the bottom layer. Because Litz wire has limited flexibility, significant space would have to be allocated for the windings to transition between the top and bottom layers, thus reducing winding space efficiency. This contrasts with the three-phase two-layer topology, which transitions between the top and bottom layers only when moving between the negative and positive pole windings. Additionally, three-phase systems will result in cancellation of triplen harmonics, which can mitigate some electromagnetic interference issues and reduce losses associated with prominent third harmonics. Three-phase systems will also have significantly less dc-link current ripple compared to two-phase systems.

2) Five-Phase, Seven-Phase, and Higher Phase Systems: One may also consider five-phase, seven-phase, and higher phase systems. Generally, these systems will have the benefit of reduced dc-link current ripple. For planar couplers, power transfer is proportional to 1) the number of layers, and 2) the coil span of each phase. For a fixed number of layers, the coil span must decrease as additional phases are added. However, larger coil spans are generally preferred to maximize the coupling between the GA and VA. Alternatively, additional layers may be added but this will increase either the package thickness or winding voltage, and exacerbate difficulties associated with inductance imbalances. On the issue of harmonics, systems with a number of phases greater than three may be consider suboptimal in the sense that, since the third harmonic is typically the largest, it is usually desirable to cancel this one rather than the fifth or seventh if given a choice. It is not straightforward to conclude that a higher number of phases would be better or worse than a three-phase system for this type of application without further analysis.

III. Resonance Conditions

Because the magnetic coupling between GAs and VAs with a large airgap is low, the operating power factor without any capacitive compensation is rather poor. Resonant tuning is used to achieve load-independent power factor correction, which improves system efficiency. This section briefly reviews mathematical descriptions of resonance for single-phase systems, describes the basic resonant network topologies for polyphase systems, and develops methodology for their tuning.

A. Single-Phase Resonance Conditions

In single-phase systems, series resonant networks are characterized by the property of zero impedance at the resonant frequency. Let $Z(\omega)$ represent the frequency-dependent impedance. Then, the resonant conditions for single-phase systems (assuming no losses) can be expressed as

$$Z(\omega) = 0. \tag{18}$$

An alternative interpretation of this condition is that maintaining a sinusoidal current through an unloaded single-phase series resonant network requires no input voltage. Let I be the steady-state current through the series resonant network.

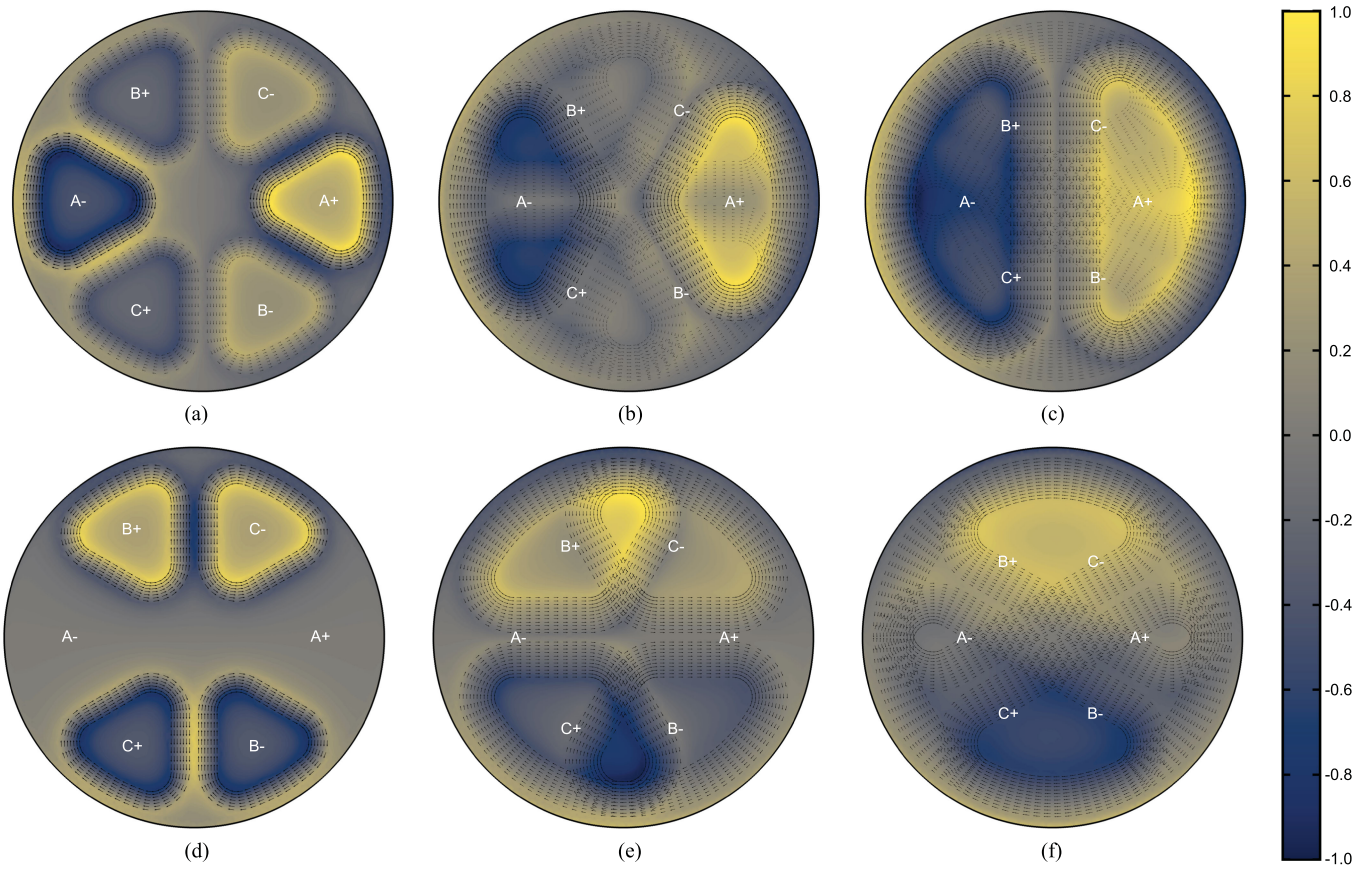

Fig. 5. Bipolar three-phase coil system α and β excitation modes. The plots depict the z-component of the flux density on the surface of the ferrite along with arrows representing the magnitude and direction of the impressed current density. The plots are normalized pairwise relative to the maximum flux density occurring in the α excitation mode for each coil configuration. (a) Single-layer α-axis excitation. (b) Double-layer α-axis excitation. (c) Triple-layer α-axis excitation. (d) Single-layer β-axis excitation. (e) Double-layer β-axis excitation. (f) Triple-layer β-axis excitation.

Then, the previous statement can be expressed as

$$Z(\omega) I = 0. \tag{19}$$

Given (18), it may seem unnecessary to explicitly state (19). However, the interpretation of resonance as a relationship between steady-state voltage and current is important for understanding polyphase resonant circuits.

B. Polyphase Resonance Conditions

For polyphase systems, the resonant conditions in (19) can be restated as

$$\underline{\mathbf{Z}}(\omega) \mathbf{I} = 0 \tag{20}$$

where $\underline{\mathbf{Z}}$ is the polyphase impedance matrix, and $\mathbf{I}$ is a vector of currents. Because (20) is a vector equation, the interpretation of polyphase resonance is more complex.

First, a resonant frequency is not necessarily restricted to one that makes $\underline{\mathbf{Z}}(\omega) = \underline{\mathbf{0}}$ (i.e., the zero matrix). Rather, ω is a resonant frequency of $\underline{\mathbf{Z}}(\omega)$ if there exists some vector $\mathbf{u}$ such that the pair $(\omega, \mathbf{u})$ satisfies $\underline{\mathbf{Z}}(\omega)\mathbf{u} = 0$. This is the same as saying that ω is a resonant frequency of the network if $\underline{\mathbf{Z}}(\omega)$ has a nontrivial null space. Equivalently, one can say $\underline{\mathbf{Z}}(\omega)$ has at least one eigenvalue equal to zero. In this context, $\mathbf{u}$ is understood to be an eigenvector of $\underline{\mathbf{Z}}(\omega)$ associated with an eigenvalue that is equal to zero.

Second, unique resonant modes of the circuit may exist at the same or different frequencies. A circuit having multiple resonant frequencies is a familiar idea. A unique property of polyphase resonant systems is that each resonant frequency has a set of mode shapes associated with the null space of the impedance matrix. These mode shapes are the eigenvectors associated with the zero-valued eigenvalues. When two or more linearly independent vectors satisfy (20) at the same frequency, then any linear combination of these vectors is also a resonant mode. When this is the case, multiple resonant modes may be excited simultaneously.

Third, the capacitors and inductors in three-phase resonant networks may be connected in various combinations of delta and wye configurations. This leads to a total of four different series compensation networks. The choice of resonant network provides an additional degree of freedom in managing voltage and current ratings among tuning components, switches, and coils. Certain topologies may also yield packaging benefits for highly optimized commercial products. In the following discussion of series tuning, the three-phase capacitances will

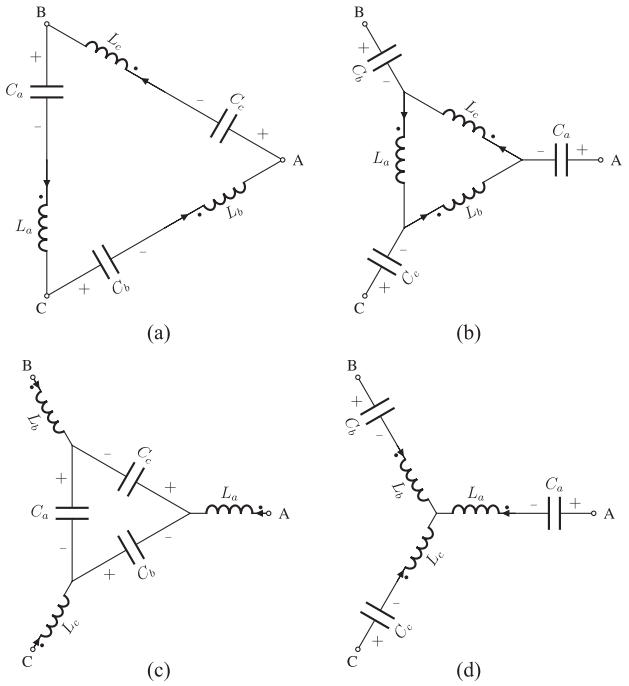

Fig. 6. Three-phase series resonant network topologies. (a) Series ΔC-ΔL. (b) Series YC-ΔL. (c) Series ΔC-YL. (d) Series YC-YL.

be represented by the following matrix:

$$\underline{\mathbf{C}} = \begin{bmatrix} C_a & 0 & 0 \\ 0 & C_b & 0 \\ 0 & 0 & C_c \end{bmatrix}. \tag{21}$$

The admittance matrix associated with the capacitors is denoted as $\underline{\mathbf{Y}}_C = j\omega\underline{\mathbf{C}}$.

C. Three-Phase Series Compensation Networks

The four different three-phase series resonant compensation topologies are shown in Fig. 6. It is clear that the capacitors are in series with the inductors in Fig. 6(a) and (d); the only difference is that the series-compensated branches are connected in wye or delta. If the delta–wye transformation is applied to the loops in Fig. 6(b) and (c), these circuits can also be viewed as part of a series compensation network. The ac circuit equations for the resonant networks can be stated simply using block-matrix notation considering the line-to-line voltages as the driving source.

1) Series ΔC-ΔL [Fig. 6(a)]:

$$\begin{bmatrix} \underline{\mathbf{P}}\mathbf{Z}_L & \underline{\mathbf{P}} \\ -\underline{\mathbf{I}} & \underline{\mathbf{Y}}_C \end{bmatrix} \begin{bmatrix} \mathbf{I}_L \\ \mathbf{V}_C \end{bmatrix} = \begin{bmatrix} \mathbf{V}_{ll} \\ \mathbf{0} \end{bmatrix}. \tag{22}$$

2) Series YC-ΔL [Fig. 6(b)]:

$$\begin{bmatrix} \underline{\mathbf{P}}\mathbf{Z}_L & \underline{\mathbf{D}}_Y \\ -\underline{\mathbf{D}}_\Delta & \underline{\mathbf{Y}}_C \end{bmatrix} \begin{bmatrix} \mathbf{I}_L \\ \mathbf{V}_C \end{bmatrix} = \begin{bmatrix} \mathbf{V}_{ll} \\ \mathbf{0} \end{bmatrix}. \tag{23}$$

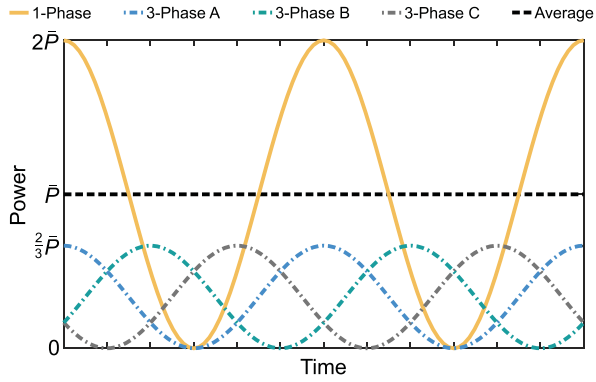

Fig. 7. Comparison of idealized instantaneous power characteristics of single-phase and three-phase WPT systems. Single-phase systems exhibit peak power that is twice that of the average. In three-phase systems, each phase exhibits peak power that is two-thirds of the average power, whereas the total instantaneous energy transfer rate is constant.

3) Series ΔC-YL [Fig. 6(c)]:

$$\begin{bmatrix} \underline{\mathbf{D}}_Y\underline{\mathbf{Z}}_L & \underline{\mathbf{P}} \\ -\underline{\mathbf{I}} & \underline{\mathbf{D}}_\Delta\underline{\mathbf{Y}}_C \end{bmatrix} \begin{bmatrix} \mathbf{I}_L \\ \mathbf{V}_C \end{bmatrix} = \begin{bmatrix} \mathbf{V}_{ll} \\ \mathbf{0} \end{bmatrix}. \tag{24}$$

4) Series YC-YL [Fig. 6(d)]:

$$\begin{bmatrix} \underline{\mathbf{D}}_Y\underline{\mathbf{Z}}_L & \underline{\mathbf{D}}_Y \\ -\underline{\mathbf{I}} & \underline{\mathbf{Y}}_C \end{bmatrix} \begin{bmatrix} \mathbf{I}_L \\ \mathbf{V}_C \end{bmatrix} = \begin{bmatrix} \mathbf{V}_{ll} \\ \mathbf{0} \end{bmatrix}. \tag{25}$$

IV. $\alpha\beta\gamma$ Resonant Tuning Analysis

This section uses the Clarke transformation to positively construct resonant modes through the choice of tuning capacitor values. It will be shown that, for any of the previously described resonant networks, α and β components can be made resonant modes of the system at a single frequency. Once tuned, α and β modes of a WPT system can be excited in quadrature to produce a resonant rotating magnetic field to achieve high-efficiency constant power transfer. A comparison between single-phase and three-phase rotating magnetic field WPT systems is depicted in Fig. 7.

A. Tuning Methodology

To determine capacitor values that make α and β modes resonant modes of the system, the impedance matrix relating the phase currents to the applied line-to-line voltages is calculated. To do this, all capacitor voltages must be eliminated from the circuit equations. The zero-sequence inductor current should also be eliminated if possible. The impedance matrix appearing in the reduced set of circuit equations is calculated using the Schur complement technique [41].

The following generic form can be used to refer to all circuit equations represented by (22)–(25):

$$\underline{\mathbf{A}}^{abc}\mathbf{x} = \mathbf{b}. \tag{26}$$

The matrix $\underline{\mathbf{A}}^{abc}$ is given by

$$\underline{\mathbf{A}}^{abc} = \begin{bmatrix} \underline{\mathbf{A}}_{1,1} & \underline{\mathbf{A}}_{1,2} \\ \underline{\mathbf{A}}_{2,1} & \underline{\mathbf{A}}_{2,2} \end{bmatrix}. \tag{27}$$

TABLE I
SERIES TUNING CIRCUIT EQUATION SUBMATRICES

Topology	Equation	$\underline{\mathbf{A}}_{1,1}$	$\underline{\mathbf{A}}_{1,2}$	$\underline{\mathbf{A}}_{2,1}$	$\underline{\mathbf{A}}_{2,2}$
ΔC-ΔL	(22)	$\underline{\mathbf{P}}\underline{\mathbf{Z}}_L$	$\underline{\mathbf{P}}$	$-\underline{\mathbf{I}}$	$\underline{\mathbf{Y}}_C$
YC-ΔL	(23)	$\underline{\mathbf{P}}\underline{\mathbf{Z}}_L$	$\underline{\mathbf{D}}_Y$	$-\underline{\mathbf{D}}_\Delta$	$\underline{\mathbf{Y}}_C$
ΔC-YL	(24)	$\underline{\mathbf{D}}_Y\underline{\mathbf{Z}}_L$	$\underline{\mathbf{P}}$	$-\underline{\mathbf{I}}$	$\underline{\mathbf{D}}_\Delta\underline{\mathbf{Y}}_C$
YC-YL	(25)	$\underline{\mathbf{D}}_Y\underline{\mathbf{Z}}_L$	$\underline{\mathbf{D}}_Y$	$-\underline{\mathbf{I}}$	$\underline{\mathbf{Y}}_C$

The specific values of the $\underline{\mathbf{A}}_{i,j}$ submatrices with respect to (22)–(25) are summarized in Table I.

The unknown vector $\mathbf{x}$ is given by

$$\mathbf{x} = \begin{bmatrix} \mathbf{I}_L & \mathbf{V}_C \end{bmatrix}^T. \tag{28}$$

The forcing vector $\mathbf{b}$ is given by

$$\mathbf{b} = \begin{bmatrix} \mathbf{V}_{ll} & \mathbf{0} \end{bmatrix}^T. \tag{29}$$

To calculate the reduced dimension impedance matrices, $\underline{\mathbf{A}}^{abc}$ is first transformed into the $\alpha\beta\gamma$ reference frame as $\underline{\mathbf{A}}^{\alpha\beta\gamma} = \underline{\mathbf{T}}\underline{\mathbf{A}}^{abc}\underline{\mathbf{T}}^T$. Then, $\underline{\mathbf{A}}^{\alpha\beta\gamma}$ is partitioned as

$$\underline{\mathbf{A}}^{\alpha\beta\gamma} = \begin{bmatrix} \underline{\mathbf{U}} & \underline{\mathbf{V}} \\ \underline{\mathbf{W}} & \underline{\mathbf{X}} \end{bmatrix}. \tag{30}$$

The partition is defined implicitly by the condition that $\underline{\mathbf{X}}$ be the largest invertible submatrix of $\underline{\mathbf{A}}^{\alpha\beta\gamma}$ with dimension 4 or less. The general expression for the reduced dimension impedance matrix is

$$\underline{\mathbf{Z}} = \underline{\mathbf{U}} - \underline{\mathbf{V}}\underline{\mathbf{X}}^{-1}\underline{\mathbf{W}}. \tag{31}$$

The matrix $\underline{\mathbf{X}}$ must be invertible to calculate $\underline{\mathbf{Z}}$. If all the capacitor voltages and the common-mode current can be eliminated from the equations, then $\underline{\mathbf{X}}$ of dimension 4 is invertible. If the common-mode current cannot be eliminated, then $\underline{\mathbf{X}}$ of dimension 4 is noninvertible and therefore must be restricted to dimension 3.

The matrix $\underline{\mathbf{X}}$ associated with (22)–(24) is dimension 4. The matrix $\underline{\mathbf{X}}$ associated with (25) is dimension 3. To understand why the dimension 4 submatrix for the YC-YL circuit is not invertible, note that the entire first block row of (25) is premultiplied by $\underline{\mathbf{D}}_Y$. The explicit representation of $\underline{\mathbf{D}}_Y$ in the $\alpha\beta\gamma$ reference frame is given by

$$\underline{\mathbf{D}}_Y^{\alpha\beta\gamma} = \underline{\mathbf{T}}\underline{\mathbf{D}}_Y^{abc}\underline{\mathbf{T}}^T = \frac{1}{2}\begin{bmatrix} 3 & -\sqrt{3} & 0 \\ \sqrt{3} & 3 & 0 \\ 0 & 0 & 0 \end{bmatrix}. \tag{32}$$

Therefore, $\underline{\mathbf{A}}^{\alpha\beta\gamma}$ has a vector of zeros associated with the zero-sequence voltage occurring in the third row of the matrix. Intuitively, this occurs because the zero-sequence voltage is not observable from the line-to-line voltages in a wye-connected load with a floating neutral point.

Now let $z_{m,n}$ denote the entries of the matrix $\underline{\mathbf{Z}}$. To determine the resonant capacitor values that make α and β modes resonant, the equations $z_{1,1} = z_{1,2} = z_{2,1} = z_{2,2} = 0$ must be solved. In other words, the 2×2 submatrix in the upper left corner of $\underline{\mathbf{Z}}$ should equal zero. MATLAB's symbolic computing toolbox has been used to perform the calculations. The script is included with this article's supplemental material.

B. Series Tuning Capacitor Expressions

This section presents the solutions to the equations described in Section IV-A. First, a few intermediate variables are introduced to reduce the complexity of the resulting expressions. In the following, the set of indices $\{i, j, k\}$ may be equal to any cyclical permutation of $\{a, b, c\}$.[2]

Variables L_i^γ are intermediate inductances associated with the Y-connected inductor systems

$$L_i^\gamma = L_i - M_{ij} + M_{jk} - M_{ki}. \tag{33}$$

Similarly, variables L_i^δ are intermediate inductances associated with the Δ-connected inductor systems

$$L_i^\delta = L_i + M_{ij} + M_{ki}. \tag{34}$$

The sum of all L_i^δ is denoted as

$$L^\sigma = L_a^\delta + L_b^\delta + L_c^\delta. \tag{35}$$

Finally, significant simplifications occur when the system has balanced inductances. Let L and M represent the unique self- and mutual inductances in a balanced coupled inductor system. That is, $L = L_a = L_b = L_c$ and $M = M_{ab} = M_{bc} = M_{ca}$. Let L' be the effective inductance associated with balanced systems

$$L' = L - M. \tag{36}$$

1) Series ΔC-ΔL [Fig. 6(a)]:

$$\omega^2 C_i = \begin{cases} \dfrac{1}{L'} & \text{balanced} \\ \dfrac{M_{jk}}{L_i M_{jk} - M_{ij} M_{ki}} & \text{unbalanced.} \end{cases} \tag{37}$$

2) Series YC-ΔL [Fig. 6(b)]:

$$\omega^2 C_i = \begin{cases} \dfrac{3}{L'} & \text{balanced} \\ \dfrac{L^\sigma}{L_j^\delta L_k^\delta - L^\sigma M_{jk}} & \text{unbalanced.} \end{cases} \tag{38}$$

3) Series ΔC-YL [Fig. 6(c)]:

$$\omega^2 C_i = \begin{cases} \dfrac{1}{3L'} & \text{balanced} \\ \dfrac{L_i^\gamma}{L_i^\gamma L_j^\gamma + L_j^\gamma L_k^\gamma + L_k^\gamma L_i^\gamma} & \text{unbalanced.} \end{cases} \tag{39}$$

4) Series YC-YL [Fig. 6(d)]:

$$\omega^2 C_i = \begin{cases} \dfrac{1}{L'} & \text{balanced} \\ \dfrac{1}{L_i^\gamma} & \text{unbalanced.} \end{cases} \tag{40}$$

[2]There are three cyclical permutations: $\{a, b, c\}$, $\{b, c, a\}$, and $\{c, a, b\}$.

TABLE II
BIPOLAR THREE-PHASE THREE-LAYER INDUCTANCES (μH)

L_a	L_b	L_c	M_{ab}	M_{bc}	M_{ca}
260	245	232	-117	-111	-110

TABLE III
BIPOLAR THREE-PHASE THREE-LAYER TUNING CAPACITORS (nF)

	ΔC-ΔL	YC-ΔL	ΔC-YL	YC-YL
C_a	9.30	30.8	3.43	9.30
C_b	9.65	30.2	3.30	9.65
C_c	10.42	27.7	3.05	10.43
$\bar{C}$	9.79	29.5	3.26	9.79

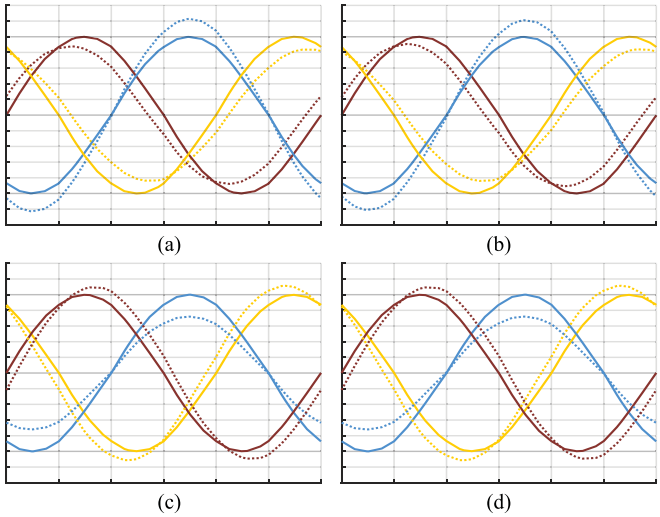

Fig. 8. Simulated steady-state primary side line-current waveforms using the bipolar three-layer three-phase system with unbalanced intra-assembly mutual inductances; the line-current amplitudes are normalized (0.2 p.u./div) with one 85-kHz period shown (0.167 periods/div). (a) ΔC-ΔL. (b) YC-ΔL. (c) ΔC-YL. (d) YC-YL.

C. Simulation Validation of Capacitor Tuning Expressions

This section validates the tuning capacitor expression from Section IV-B using inductances from the simulated three-phase three-layer bipolar WPT coupler presented in Section V. The GA inductances are given in Table II. The tuning capacitor values for each topology are given in Table III along with the average capacitor value $\bar{C}$. A maximum deviation of about 12% is observed in the calculated capacitances. All of these topologies were simulated in PLECS using 1) the capacitor values calculated from Section IV-B and 2) the average capacitor value $\bar{C}$ for each phase.

A comparison of the resulting line currents (on a per-unit basis) is given in Fig. 8. The simulations using the capacitor values calculated from Section IV-B result in perfectly balanced and 120° phase shifted line currents. In contrast, using the average capacitance value $\bar{C}$ for all three phases results in line currents with significantly different magnitudes and phases. For quantitative comparison, the normalized α- and β-mode current amplitudes were calculated in Table IV. Around a 21% difference between the maximum and minimum mode amplitude can be observed.

TABLE IV
PER-UNIT α- AND β-MODE LINE CURRENT AMPLITUDES WHEN USING THE AVERAGE TUNING CAPACITANCE $\bar{C}$ FOR EACH PHASE

	ΔC-ΔL	YC-ΔL	ΔC-YL	YC-YL
I_α	0.865	0.855	1.063	1.063
I_β	1.075	1.092	0.853	0.854

V. COMPARISON OF COIL TOPOLOGIES UNDER MAGNETIC FIELD EMISSIONS CONSTRAINTS

To demonstrate the benefits of three-phase bipolar WPT systems, we have performed a comparative design study of six different matched coupler topologies as follows:

1) single-phase unipolar 1ϕU;
2) single-phase bipolar 2ϕB;
3) three-phase unipolar with single-phase excitation 3ϕU(1ϕ);
4) three-phase unipolar with three-phase excitation 3ϕU;
5) three-phase bipolar with two layers 3ϕB;
6) three-phase bipolar with three layers 3ϕB(3L).

To focus on the impact of winding layout, we have used a circular geometry for all the couplers with a fixed outer diameter of 47 cm. The couplers use two layers of 6 AWG wire except for the three-layer three-phase system, which uses 10 AWG. This modification was made in attempt to normalize the upper bound of total Litz wire mass and keep the package thickness similar between systems.

Practical vehicle charging WPT systems must meet stringent requirements for electromagnetic field emissions as described by the International Commission on Non-Ionizing Radiation Protection (ICNIRP) as referenced by Society of Automotive Engineers's (SAE's) J2954 [42]. SAE J2954 also describes various foreign object heating and ignition tests that a system must pass either through the use of a foreign object detection (FOD) systems or by limiting the maximum flux density on the surface of the GA package. It can be difficult or prohibitively expensive to design a FOD system capable of detecting small objects such as coins or paperclips. In practice, the peak flux density on the surface of the GA package must be limited to meet the touch safety requirements described in SAE J2954.

Safety considerations with respect to emissions and foreign object heating severely limit the maximum power capability of WPT systems with a given coupler size. Our approach in the design of the six couplers was to maximize the power capability while keeping the peak magnetic field occurring at a distance of 80 cm from the center of the GA/VA system below 21.2 μT, which is the level specified by ICNIRP for pacemaker compatibility. This is accomplished by adjusting 1) the number of turns and 2) the spacing between the turns. The backing ferrite thickness was adjusted to keep the peak flux density below 200 mT. Table V summarizes the final design parameters of the six coupler topologies.

A comparison of the magnetic field emissions, $B_{\max} = \max_t \|B(t)\|$, is given in Fig. 9. All couplers exhibit peak field emissions that are slightly below 21.2 μT level. Four of the couplers—1ϕU, 3ϕU(1ϕ), 3ϕB, 3ϕB(3L)—exhibit emissions profiles that are nearly constant with respect to angular

TABLE V
COIL DESIGN PARAMETERS WITH FIXED OUTER DIAMETER OF 47 cm

Topology	Wire Gauge (AWG)	Turns (1)	Turn Spacing (mm)	Winding Thickness (mm)	Ferrite Thickness (mm)
1φU	6	5	38.7	12.6	2.31
1φB	6	8	16.1	12.6	6.03
3φU(1φ)	6	4	15.0	12.6	2.36
3φU	6	6	11.3	12.6	7.00
3φB	6	8	8.8	12.6	6.32
3φB(3L)	10	16	5.3	11.4	6.90

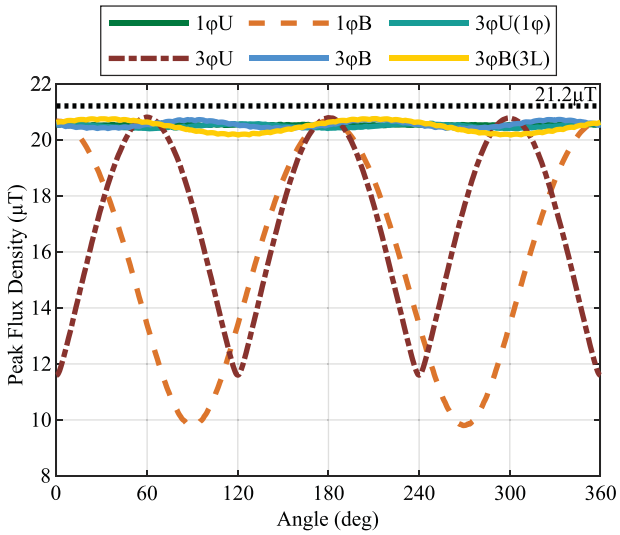

Fig. 9. Maximum flux density at a distance of 80 cm from the center of the GA/VA airgap.

displacement at 80 cm from the GA/VA airgap center. The 1ϕB and 3ϕU couplers exhibit spatial harmonic variations in the emissions having periods 2 and 3, respectively.

Table VI compares several performance metrics for the coupler topologies. Of the single-phase excited system, the bipolar coupler is able to achieve the highest power transfer rate under the emissions constraint. This indicates that the bipolar coupler has better emission characteristics than unipolar couplers. The couplers utilizing three-phase excitation are able to achieve higher power levels for these emissions constraints. The bipolar three-phase couplers combine the uniform emissions profile of the single-phase unipolar coupler with the overall lower emissions characteristics of the single-phase bipolar coupler. Post processing loss estimates reveal that all of the topologies—except for 3ϕU(3ϕ)—are very similar in terms of efficiency. The reason for the lower efficiency of the 3ϕU(3ϕ) topology is that adjacent phase winding sections extending in the radial direction produce flux in opposing directions, resulting in less effective use of the windings. Flux cancellation is one motivating factor behind the decoupling of the windings in the tripolar coupler design [21].

The three-phase bipolar couplers achieve better specific power than the single-phase bipolar coupler and approach that of the single-phase unipolar coupler. The 3ϕB(3L) topology is nearly as good as that of 1ϕU by this metric. The copper mass of the Litz wire tracks the power rating of the coils fairly closely. Most of the difference in specific power between the topologies can be traced to the mass of the ferrites. To explore this issue in more depth, the maximum flux density in the ferrites of each coupler is plotted in Fig. 10. The improved specific power of the 1ϕU, 3ϕB, and 3ϕB(3L) couplers can be attributed to the better ferrite utilization of these topologies. In contrast, the 1ϕB, 3ϕU(1ϕ), and 3ϕU topologies have prominent regions where the maximum flux density is significantly below 200 mT limit. As a result, the former topologies must have thicker backing ferrites for a given power to avoid magnetic saturation.

To determine how the topologies might perform with respect to foreign object heating constraints, we have analyzed the magnetic fields on the surface of the GA, which is assumed to be 6 cm above the bottom of the ferrites. The comparison is performed by examining the ratio P/B_{max}^2 in Table VI, where P is the power transfer and B_{max} is the peak flux density on the surface of the GA. The term B_{max}^2 is proportional to the amount of eddy-current heating that would occur in a small metallic object placed on the surface of the GA at the maximum flux density location. Larger values of this ratio indicate that a given system should be capable of transferring more power before reaching foreign object heating and touch safety limitations. The 3ϕB topology has the best performance by this metric, followed closely by the 3ϕB(3L) design. The reason for the improved performance of the three-phase topologies can be understood by examining the GA surface flux density plots in Fig. 11. The single-phase and 3ϕU topologies exhibit concentrated flux density "hot spots." The 3ϕB and 3ϕB(3L) designs achieve more uniform surface flux density distributions, which improves the P/B_{max}^2 ratio.

Finally, the wire gauge was decreased in the three-layer design to keep the total winding thickness relatively constant between the 3ϕB and 3ϕB(3L) topologies. This has the drawback of requiring a large increase in the winding voltage to achieve the same power. In practice, the maximum permissible winding voltage may be limited for safety. If this is the case, using the 3ϕB(3L) topology may require the winding thickness to increase by 50 % beyond the 3ϕB topology. This consideration must be weighed against the potential for improving power density and specific power when using the 3ϕB(3L) coupler.

VI. PROTOTYPE SYSTEM

Prototype couplers based on the two-layer winding topology were constructed for experimental validation. This topology was chosen because it results in the system with the largest coil span having balanced inductances. Although resonant tuning can be performed for a system with unbalanced inductances, it is difficult to realize the exact required capacitance values with monolithic induction heating capacitors having high kVA ratings. Rather, low kVA discrete components need to be combined to realize the appropriate capacitances. For systems with balanced inductances, the capacitors can be chosen to locate the actual system resonant frequency as near as possible to the target frequency.

TABLE VI
COMPARISON OF DIFFERENT COIL TOPOLOGIES DESIGNED UTILIZING A MAXIMUM DIAMETER OF 47 cm AND MAXIMUM MAGNETIC FIELD EMISSIONS AMPLITUDE OF 21.2 μT AT 80 cm FROM THE CENTER OF THE SYSTEM

Topology	Power (kW)	Copper Mass (kg)	Ferrite Mass (kg)	Specific Power (kW kg^{-1})	Copper Loss (W)	Ferrite Loss (W)	Efficiency (%)	Surface Flux (mT)	$\frac{P}{B^2_{max}}$ (pu)	Phase Voltage (kV_{RMS})
1φU	24.5	1.03	1.92	8.31	72	59	98.93	5.09	0.679	1.39
1φB	36.6	1.67	5.70	4.97	117	66	99.00	6.69	0.587	2.98
3φU(1φ)	14.7	1.80	1.96	3.91	125	41	97.74	3.85	0.712	0.69
3φU	49.3	2.47	5.83	5.94	172	91	98.93	8.26	0.835	1.74
3φB	62.7	3.19	5.02	7.64	222	108	98.95	6.71	1.000	1.79
3φB(3L)	75.1	3.44	5.75	8.17	240	108	99.07	7.44	0.974	5.33

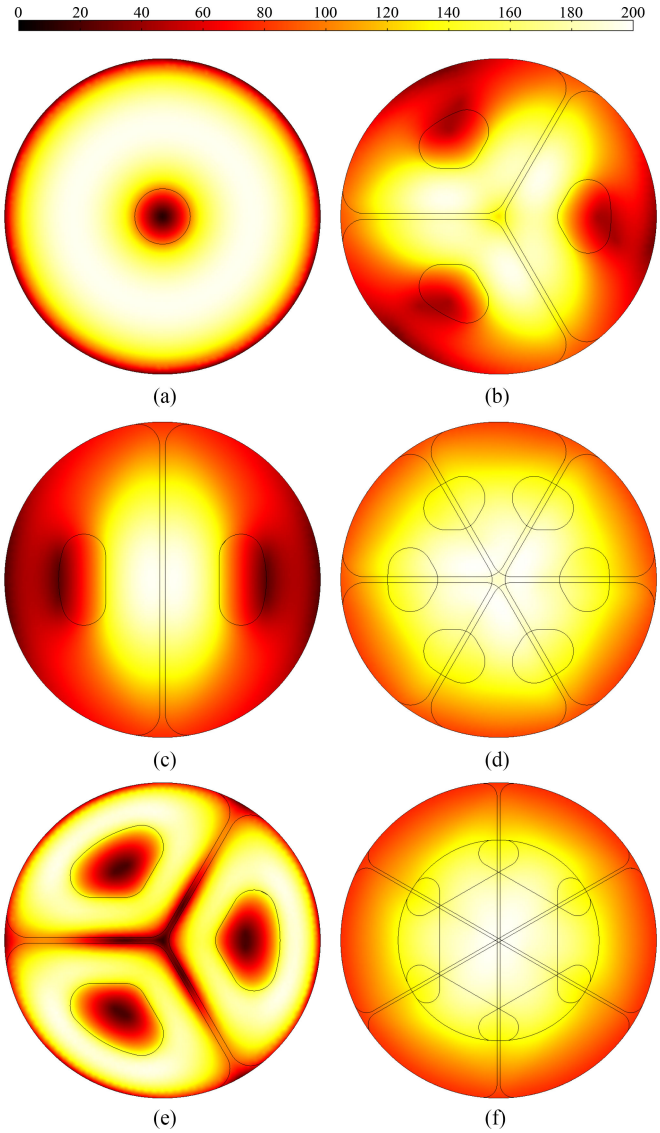

Fig. 10. Maximum flux density in the ferrites (mT). (a) 1ϕU. (b) 3ϕU. (c) 1ϕB. (d) 3ϕB. (e) 3ϕU(1ϕ). (f) 3ϕB(3L).

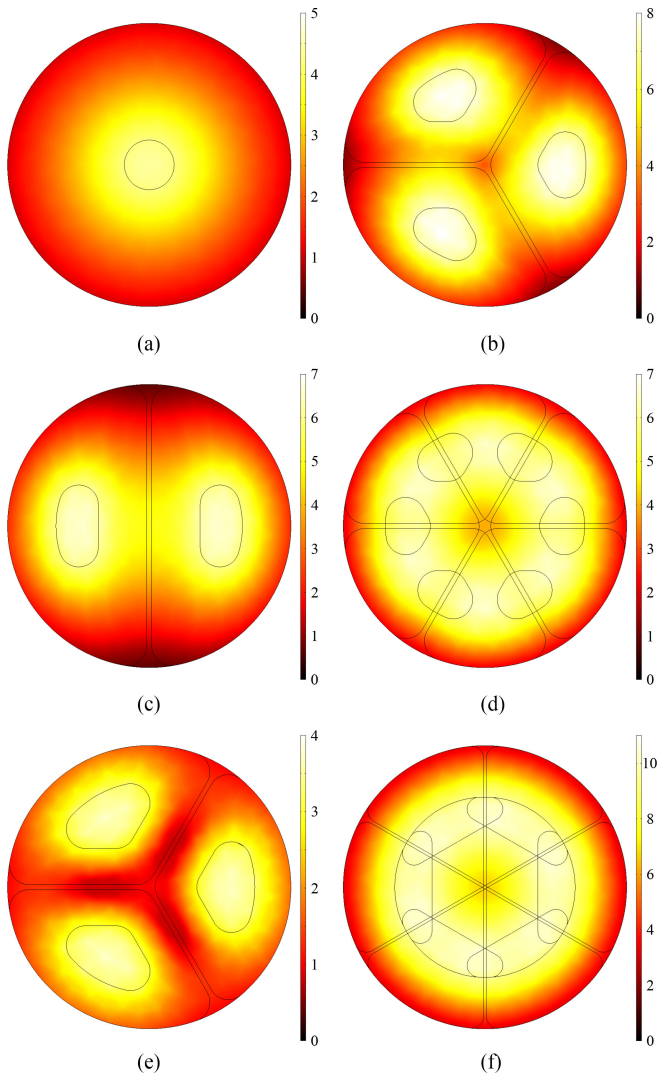

Fig. 11. Maximum flux density at distance of 6 cm from the bottom of the GA. All scales are in mT. (a) 1ϕU. (b) 3ϕU. (c) 1ϕB. (d) 3ϕB. (e) 3ϕU(1ϕ). (f) 3ϕB(3L).

A. Couplers

A computational model and the physical prototype of the two-layer three-phase coil system are depicted in Figs. 12 and 13, respectively. The initial design of the pad targeted an effective mutual inductance to achieve 50 kW power transfer for a coupler surface-to-surface separation of 15 cm and a phase current of 73 A_{RMS}. This current corresponds to a current density of 5.5 A_{RMS}/mm^2 in 6 AWG wire. The design was limited by the 7.4 mm diameter of the Litz wire and the minimum

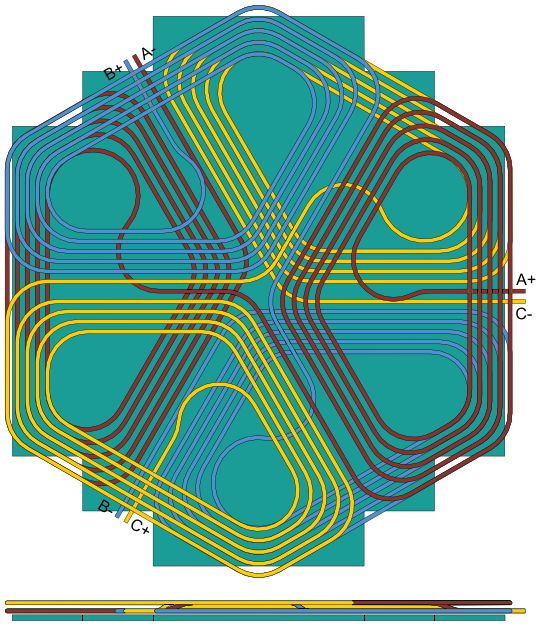

Fig. 12. Two-layer coupler design. The simulation model gives details of the phase winding layout including location of terminals and mechanics for routing the wires to connect the top and bottom layers. The diameter of the Litz wire is scaled to reduce meshing complexities.

Fig. 13. Two-layer coupler prototype. The bounding box of the pad is 47.1 cm × 54.4 cm. The total coil mass including ferrite, Litz wire, and wire guides is 13.7 kg. The wire is 6 AWG type 2 Litz with a strand gauge of 38 AWG produced by New England Wire. The ferrite backing is constructed from Ferroxcube PLT64/50/5 tiles of 3C94 material.

bend radius, which was set to be five times the diameter. A minimum wall thickness of 1.8 mm for mechanical integrity of the additively manufactured wire guides also limited space for additional amp-turns. The resulting system has a VA ground clearance of 170 mm and a magnetic airgap of 180 mm. A full

TABLE VII
COUPLER INDUCTANCES (μH) FOR COIL-TO-COIL DISTANCE OF 15 cm AND VA GROUND CLEARANCE OF 17 cm

		Aligned		$\Delta\varphi$=30°		Δx=–10 cm Δy=+10 cm	
		Sim.	Exp.	Sim.	Exp.	Sim.	Exp.
GA Self–inductances	L_a	34.1	31.7	34.1	30.9	33.8	30.4
	L_b	34.3	31.8	34.3	30.6	33.9	30.2
	L_c	34.2	31.7	34.2	30.9	34.0	30.8
	M_{ab}	-11.2	-10.5	-11.2	-10.2	-11.0	-10.2
	M_{bc}	-11.3	- 9.8	-11.3	- 9.9	-11.1	- 9.7
	M_{ca}	-11.1	-10.5	-11.1	-10.0	-11.1	-10.5
VA Self–inductances	L_a	34.1	31.6	34.1	30.7	33.7	30.6
	L_b	34.2	32.0	34.2	31.0	33.8	30.8
	L_c	34.3	31.6	34.3	30.9	34.1	30.7
	M_{ab}	-11.1	-10.0	-11.1	-10.6	-10.8	- 9.9
	M_{bc}	-11.3	-10.4	-11.3	-10.2	-11.2	- 9.4
	M_{ca}	-11.2	- 9.9	-11.2	- 9.6	-11.2	- 9.7
GA to VA Mutual–inductances	M_{ga}^{va}	5.65	4.55	5.32	5.40	3.20	3.00
	M_{ga}^{vb}	-1.85	-1.27	-4.29	-3.97	0.38	0.46
	M_{ga}^{vc}	-3.65	-3.32	-1.08	-1.47	-3.33	-3.35
	M_{gb}^{va}	-3.65	-3.40	-1.08	-1.73	-0.89	-0.73
	M_{gb}^{vb}	5.54	4.96	5.20	5.42	1.33	1.04
	M_{gb}^{vc}	-1.77	-2.30	-4.18	-3.57	-0.68	-0.27
	M_{gc}^{va}	-1.85	-1.15	-4.29	-3.27	-1.98	-1.40
	M_{gc}^{vb}	-3.57	-3.67	-0.99	-1.49	-1.97	-2.08
	M_{gc}^{vc}	5.54	5.27	5.20	5.11	3.80	3.93

TABLE VIII
THEORETICAL CAPACITOR VALUES AND RATINGS FOR DIFFERENT 85 kHz RESONANT FREQUENCY COMPENSATION NETWORKS

	C (nF)		V (V_{RMS})		I (A_{RMS})	
	Sim.	Exp.	Sim.	Exp.	Sim.	Exp.
ΔC-ΔL	77.7	83.1	1764	1649	73.2	
YC-ΔL	230.0	255.9	1032	927	126.7	
ΔC-YL	25.6	28.4	3087	2782	42.2	
YC-YL	77.7	81.7	1764	1678	73.2	

The calculated values are based on the inductances in Table VII for phase A of the GA in the aligned case.

3-D model of the pad has been included in the supplemental material as a 3-D PDF.

Table VII compares the measured coupler inductances to those simulated in COMSOL using the model in Fig. 12 under three different alignment conditions depicted in Fig. 14: perfectly aligned, aligned with a 30° rotation, and offset by 10 cm in both the x and y directions. Management of the phase leads makes measurement of the inductances challenging. This likely is a large contributor to the observed discrepancies between the simulations and measurements. Additionally, there is a tradeoff between how the leads are drawn for numerical computation and the discrepancy between simulation and measurements. Drawing the return paths below and above the GA and VA, respectively, will minimize the impact on simulated GA–VA coupling, which is most important for predicting power transfer,

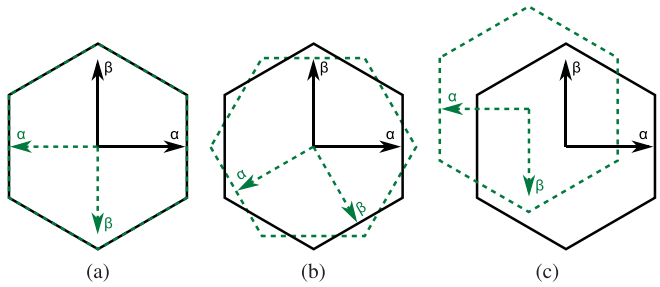

Fig. 14. Three different alignment conditions: (a) perfectly aligned, (b) 30° rotation, and (c) −10 cm × +10 cm translational misalignment.

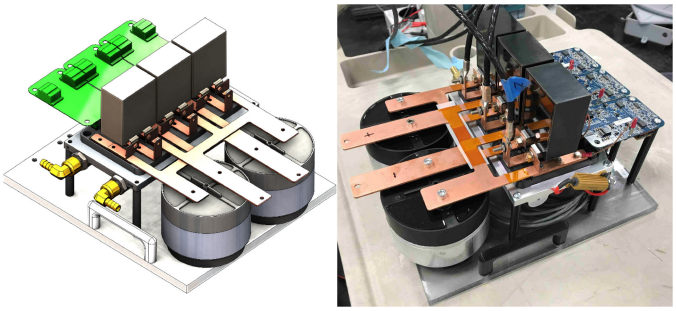

Fig. 15. 3-D rendering and photograph of the three-phase SiC inverter.

but may introduce larger errors in the self-inductances calculations than a different approach. The ideal tuning capacitors for GA phase A in the aligned case are listed in Table VIII for tuning topologies in Fig. 6.

B. Power Electronics

The inverter used to drive the system is depicted in Fig. 15. The design uses three 1200 V/325 A SiC half-bridge modules (CAS325M12HM2) and gate drivers (CGD15HB62LP) from Wolfspeed. An identical unit is used as the rectifier by setting the gate signals to turn the metal–oxide–semiconductor field-effect transistors OFF. Two 600 μF dc-link capacitors (947D601K901DCRSN) are attached to the dc-link busbars and one 3 μF snubber capacitor (SCD305K122C3Z25-F) per module. The inverter was operated in an open-loop fashion from a TMS320F28335 DSP. The deadtime was set to 600 ns. The operating frequency was chosen to achieve zero-voltage switching (ZVS) at full load in the aligned configuration.

C. Experimental Setup

A high-level circuit diagram of the experimental system is given in Fig. 16. A picture of the experimental setup is given in Fig. 17. An NHR 9300 high-voltage battery test system was used as the source. An additional NHR 9300 was used in parallel with a 14 Ω resistor bank as the load. A Teledyne Lecroy HDO8108 oscilloscope was used to capture the GA voltage and current waveforms. A Yokogawa DLM4058 oscilloscope was used to capture the VA waveforms. The oscilloscopes were operated with independent triggers, resulting in an arbitrary phase shift between the GA and VA plots presented in the following section. A Yokogawa WT1806E power analyzer was used to measure the dc input power, dc output power, and dc-to-dc efficiency of the system.

VII. Experimental Results

The performance of the system was measured for three alignment conditions using the YC-YL and YC-ΔL tuning configurations. The ΔC-ΔL network was not considered due to the possibility of large circulating currents resulting from the low impedance of the loop at resonance. The ΔC-YL network was not examined because of the large voltage and small capacitance requirement of the capacitors. It is expected that the ΔC-YL configuration would behave similarly to the YC-YL configuration. The nominal tuning capacitor values for the two examined networks are given in Table IX.

A. Aligned and Rotated Results

A summary of the experimental results for the YC-YL tuned system is given in Table X. The corresponding experimental waveforms (i.e., line-to-neutral voltages and line currents) are given in Fig. 18. As expected, the aligned and 30° rotation results are nearly identical due to the rotational invariance of the system when the GA and VA central axes are aligned. Both conditions achieve 50 kW power transfer with greater than 95 % dc-to-dc efficiency.

A summary of the experimental results for the YC-ΔL tuned system is given in Table XI. The corresponding experimental waveforms (i.e., line-to-line voltages and line currents) are given in Fig. 19. Again, the aligned and 30° rotation results are nearly identical. Both conditions demonstrate 94 % efficiency while transferring 50 kW.

Compared to the YC-YL tuning, the YC-ΔL configured system is slightly less efficient. Because the load impedance required to achieve near-unity voltage gain is about three times less than in the YC-YL case, the inverter and rectifier conduction losses are likely much higher in this configuration. The increase in conduction losses may be partially offset by a decrease in switching losses due to a lower dc-link voltage. However, the reduction in switching losses is limited due to ZVS operation of the inverter during turn-ON.

The ripples on the voltage waveforms in Fig. 18 are due to a high-frequency common-mode voltage showing up on the neutral point. Qualitatively, one can observe that the voltage ripples in each of the GA waveforms have similar magnitude, phase, and shape. A similar observation can be made regarding the VA voltage waveforms. The voltage on the VA rectifier voltage waveforms in Fig. 19 is likely due an instrumentation issue, which resulted in switching noise coupling to the leads of the V_{bc} voltage probe. The noise on this probe subsequently coupled to the V_{ab} and V_{ca} probes. The leads running from the rectifier to the oscilloscopes were much longer than those for the inverter voltages, and so were more prone to this issue. The lead routing was changed between the YC-YL and YC-ΔL experiments, which is why this behavior is not observed in Fig. 18.

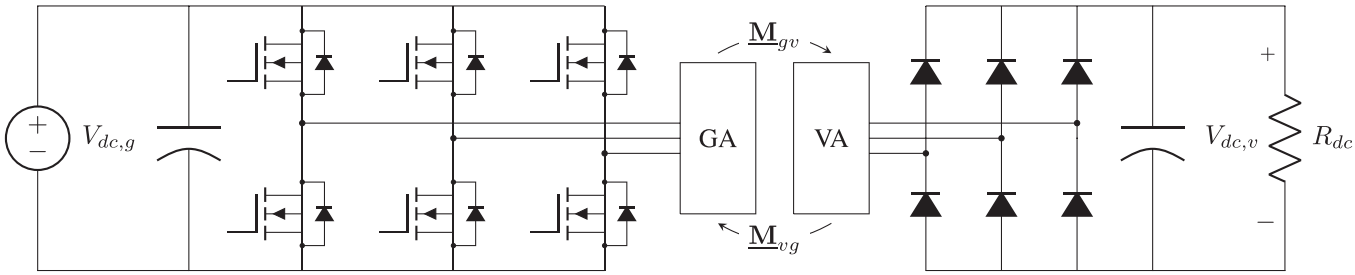

Fig. 16. System-level diagram with dc-link voltages, inverter, rectifier, and load resistance. The GA and VA blocks represent any series resonant circuit.

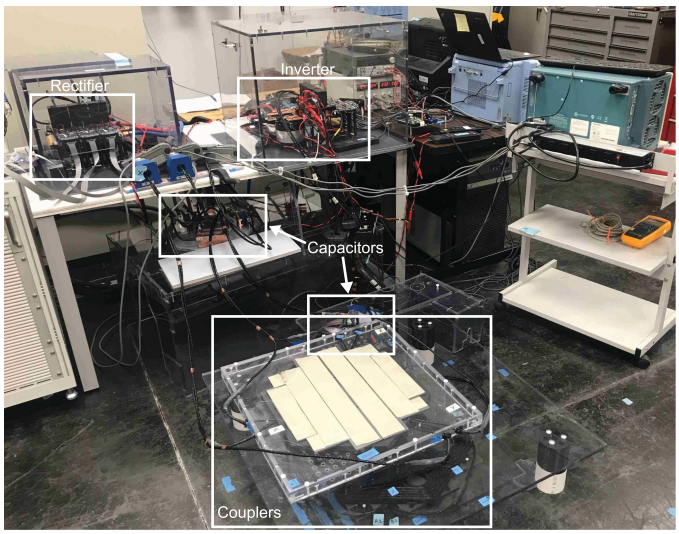

Fig. 17. Experimental setup with -10 cm $\times$ $+10$ cm misalignment.

B. Translational Misalignment Results

The performance of the system using the YC-YL and YC-ΔL tuning networks is compared in Fig. 20 when the GA and VA are misaligned by –10 cm in the *x*-direction and +10 cm in the *y*-direction. This represents a worst case scenario envisioned by the SAE J2954 recommended practice [42]. The inverter is operated using full duty cycle and 120° shifted phase legs.

In this configuration, the system power transfer capability is limited by the current rating of the coils. It can be seen in Fig. 20(a) that ground phase B supplies almost purely reactive power to the system, which is part of the cause of the reduced efficiency in the misaligned case. The poor power factor and large switching currents in the YC-ΔL system are apparent from the large voltage overshoot and ringing observed on the GA waveforms in Fig. 20(b).

Furthermore, Fig. 20 shows that the vehicle coil assembly operates in a single-phase mode for both tuning configurations. This points to an interesting phenomena; as misalignment increases, the ideal operating mode transitions from three-phase excitation to single-phase excitation. This effect is similar to that exploited to achieve the high misalignment tolerance of tripolar coils [21], [22]. More work needs to be done to understand how the optimal excitation varies with misalignment for three-phase systems with nonzero interphase mutual inductance.

TABLE IX
NOMINAL REALIZED CAPACITORS FOR THE SELECTED NETWORKS AT 85 kHz CONSTRUCTED FROM CELEM CONDUCTION-COOLED CAPACITORS (CSP 120/200) WITH NOMINAL CAPACITANCES OF 0.25 AND 0.33 μF

	C (nF)	V (V_{RMS})	Construction
YC-ΔL	267.2	1490	(0.25||0.25)-(0.25||0.33)
YC-YL	90.7	2206	0.25-0.25-0.33

TABLE X
EXPERIMENTAL RESULTS WITH THE DOUBLE-SIDED YC-YL SERIES COMPENSATION NETWORK AT A SWITCHING FREQUENCY OF 88.5 kHz

	Aligned	$\Delta\varphi$=30°	Δx=–10 cm Δy=+10 cm
$V_{dc,g}$	554.9 V	555.9 V	312.7 V
$R_{dc,v}$	6.839 Ω	6.842 Ω	6.764 Ω
$P_{g,dc}$	52.60 kW	52.53 kW	11.79 kW
$P_{v,dc}$	50.03 kW	50.02 kW	10.44 kW
$V_{dc,v}$	584.9 V	585.0 V	265.8 V
η	95.1 %	95.2 %	88.5 %

TABLE XI
EXPERIMENTAL RESULTS WITH THE DOUBLE-SIDED YC-ΔL SERIES COMPENSATION NETWORK AT A SWITCHING FREQUENCY OF 89.5 kHz

	Aligned	$\Delta\varphi$=30°	Δx=–10 cm Δy=+10 cm
$V_{dc,g}$	297.3 V	297.3 V	169.9 V
$R_{dc,v}$	2.283 Ω	2.279 Ω	2.275 Ω
$P_{g,dc}$	53.15 kW	53.34 kW	12.11 kW
$P_{v,dc}$	50.13 kW	50.25 kW	10.48 kW
$V_{dc,v}$	338.3 V	338.4 V	154.4 V
η	94.3 %	94.2 %	86.5 %

Finally, Table XII summarizes the measured line current amplitudes for each experiment to further quantify the degree of imbalance resulting from misalignment. The difference in current amplitudes may also serve to indicate the degree to which the losses are distributed among the phases, although it is difficult to disaggregate the phase losses in general due to the nonlinear nature of the ferrite losses.

C. Magnetic Field Emissions

The magnetic field emissions for the YC-YL tuned system were measured in the aligned and misaligned conditions using a Narda EHP-200A electric and magnetic field analyzer. In

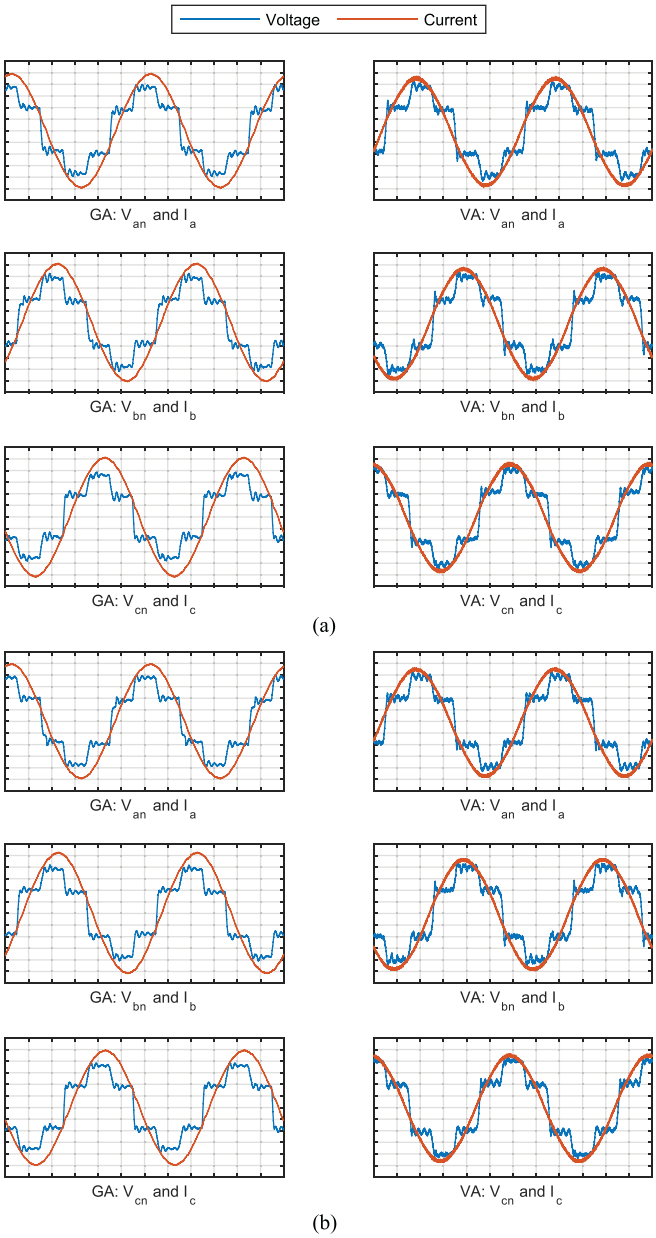

Fig. 18. Measured line currents (20 A/div) and line-to-neutral voltages (100 V/div) of the YC-YL configured three-phase system with perfect alignment and a 30° rotation; two 88.5-kHz periods are shown (1.883 μs/div). (a) Perfect alignment with 50 kW output power. (b) 30° rotation with 50 kW output power.

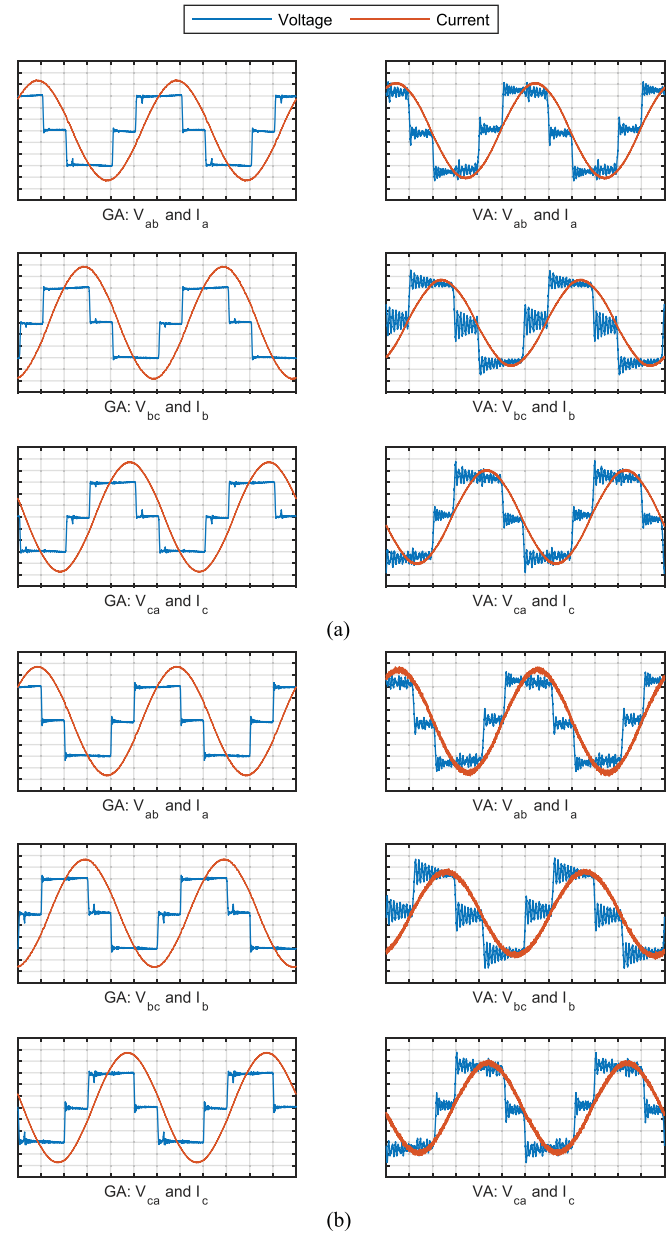

Fig. 19. Measured line currents (40 A/div) and line-to-line voltages (100 V/div) of the YC-ΔL configured three-phase system with perfect alignment and a 30° rotation; two 89.5-kHz periods are shown (1.862 μs/div). (a) Perfect alignment with 50 kW output power. (b) 30° rotation with 50 kW output power.

the aligned case, the measurement point was 80 cm from the center of the GA. In the misaligned case, the measurement point was 70 cm from the center of the GA. The measured spectra for the both cases are given in Fig. 21. The rotated case is similar to the aligned condition, with peak emissions being slightly lower in the rotated case. One challenge with magnetic field emissions measurements for polyphase systems is that proper detection of the peak field value requires the phase difference between the x, y, and z axes be taken into account. For example, a pure rotating field vector will have an rms value equal to the peak value, rather than $\sqrt{2}$ larger as with uniaxially oscillating field. However, the rms value reported out of the software ignores this information and it is not possible to precisely determine the peak magnetic field from this information alone. This phase relationship problem is identified as an issue in SAE J2954 [42].

At 50 kW in the aligned case, the magnetic field was reported to be 34.7 $\mu\mathrm{T_{RMS}}$. Depending on the component phases, this rms value could correspond to a peak value between 34.7 and 49.1 μT. This range straddles the ICNIRP-recommended level of 38.2 μT (27 $\mu\mathrm{T_{RMS}}$ nominal) for general exposure. Simulation results predicted that the peak value would be around 34.2 μT, so it is likely that the measured rms value corresponds to a peak value lower in the range. At 10.4 kW in the misaligned case, the

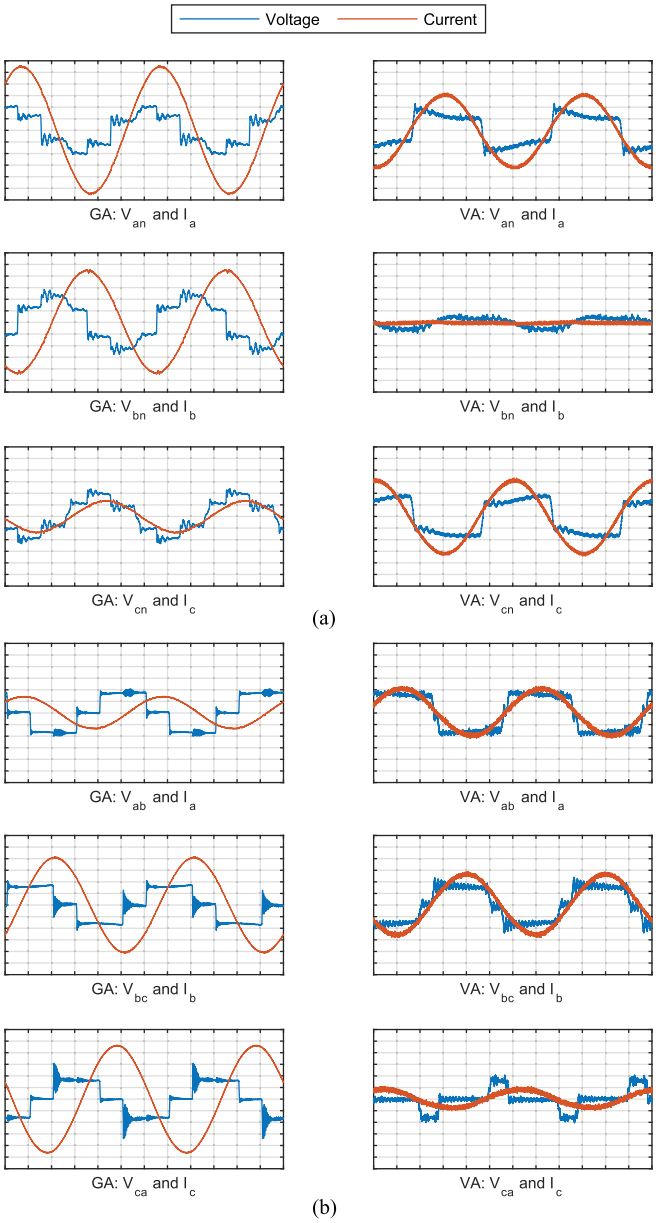

Fig. 20. Comparison of misaligned operation of the tuning configurations using 120° shifted inverter phase leg operation. (a) YC-YL configuration; 20 A/div, 100 V/div, 1.883 μs/div. (b) YC-ΔL configuration; 40 A/div, 100 V/div, 1.862 μs/div.

TABLE XII
MEASURED LINE CURRENT AMPLITUDES (A)

	Aligned		$\Delta\varphi$=30°		Δx=-10 cm Δy=+10 cm	
	YC-YL	YC-ΔL	YC-YL	YC-ΔL	YC-YL	YC-ΔL
$I_{A,g}$	99	175	99	189	111	57
$I_{B,g}$	103	195	105	187	91	167
$I_{C,g}$	103	190	100	190	29	186
$I_{A,v}$	98	166	96	188	66	92
$I_{B,v}$	100	150	99	158	6	116
$I_{C,v}$	96	164	94	165	68	44

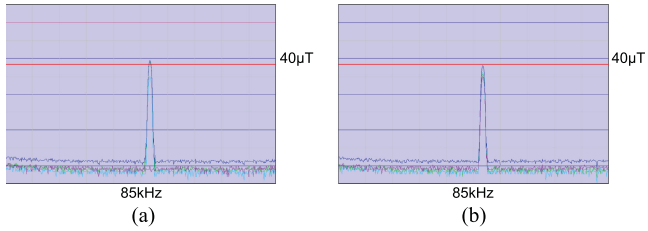

Fig. 21. Magnetic field emissions measured for two alignment conditions with central peaks located at 88.5 kHz: 11.9 kHz/div, 20 dBμT/div. (a) Aligned: 34.7 $\mu\mathrm{T_{RMS}}$. (b) Misaligned: 25.2 $\mu\mathrm{T_{RMS}}$.

reported magnetic field was 25.2 $\mu\mathrm{T_{RMS}}$, which corresponds to a peak value between 17.8 and 35.6 μT and is less than the recommended exposure level of 38.2 μT. Given the poor power factor and relatively high coil currents for this power level, it is likely that the emissions could be reduced further through proper control in misaligned conditions. It should be noted that no additional magnetic shielding was used during these tests. It is likely that the magnetic field emissions can be further reduce through a properly designed shielding system.

VIII. CONCLUSION

This article presented a three-phase WPT system capable of delivering 50 kW over a 150-mm airgap with dc-to-dc efficiency of better than 95% for the YC-YL tuning configuration and 94% for the YC-ΔL tuning configuration. High-power density is achieved through full use of the winding volume by utilizing the flux-enhancing nature of the mutual coupling between phases under three-phase excitation. Overall, system performance was similar in both tuning configurations. The choice of tuning topologies provides flexibility to match the system design to voltage, current, load, and packaging constraints for a particular application.

This article also demonstrated the difficulty that interphase mutual inductances pose when operating a system with large translational misalignment of the GA and VA. Under three-phase (120° phase shift) excitation, at least one inverter phase leg provides a large amount of reactive power, reducing efficiency. This is caused by reduced coupling between at least one pair of GA–VA phase and results in the VA coupler operating more like a traditional single-phase system. In reality, the optimal excitation in misaligned cases will be some combination of the α and β excitation modes. The method of constructing these modes needs to be examined more closely, especially for the closed-loop control operation.

ACKNOWLEDGMENT

This manuscript has been authored by UT-Battelle, LLC, under contract DE-AC05-00OR22725 with the US Department of Energy (DOE). This research used resources available at the Power Electronics and Electric Machinery Research Facility, a DOE Office of Science User Facility operated by the Oak Ridge National Laboratory (ORNL). The authors would like to thank the following people from ORNL, DOE, the National Energy

Technology Laboratory (NETL), and the National Renewable Energy Laboratory (NREL) for their contributions to this work: Randy Wiles (ORNL) for mechanical design of the inverter and rectifier assemblies; Larry Seiber (ORNL) for construction of the inverter and rectifier; Jonathan Wilkins (ORNL) for design and construction of the coil aligment system and capacitor configurations; Laurie Varma (ORNL) for technical editing support; Andrew Meintz (NREL) for reviewing an early draft of this manuscript; Burak Ozpineci and David Smith (both of ORNL) for their managerial support and technical guidance; and Lee Slezak (DOE) and Jason Conley (NETL) for funding this work and project guidance.

REFERENCES

[1] D. Howell *et al.*, Enabling Fast Charging: A Technology Gap Assessment, U.S. Department of Energy, Washington, DC, USA, Oct. 2017.

[2] G. A. Covic and J. T. Boys, "Inductive power transfer," *Proc. IEEE*, vol. 101, no. 6, pp. 1276–1289, Jun. 2013.

[3] G. A. Covic and J. T. Boys, "Modern trends in inductive power transfer for transportation applications," *IEEE J. Emer. Sel. Topics Power Electron.*, vol. 1, no. 1, pp. 28–41, Mar. 2013.

[4] J. Gao, "Traveling magnetic field for homogeneous wireless power transmission," *IEEE Trans. Power Del.*, vol. 22, no. 1, pp. 507–514, Jan. 2007.

[5] G. A. Covic, J. T. Boys, M. L. G. Kissin, and H. G. Lu, "A three-phase inductive power transfer system for roadway-powered vehicles," *IEEE Trans. Ind. Electron.*, vol. 54, no. 6, pp. 3370–3378, Dec. 2007.

[6] M. L. G. Kissin, J. T. Boys, and G. A. Covic, "Interphase mutual inductance in polyphase inductive power transfer systems," *IEEE Trans. Ind. Electron.*, vol. 56, no. 7, pp. 2393–2400, Jul. 2009.

[7] G. A. J. Elliott, S. Raabe, G. A. Covic, and J. T. Boys, "Multiphase pickups for large lateral tolerance contactless power-transfer systems," *IEEE Trans. Ind. Electron.*, vol. 57, no. 5, pp. 1590–1598, May 2010.

[8] M. L. G. Kissin, G. A. Covic, and J. T. Boys, "Steady-state flat-pickup loading effects in polyphase inductive power transfer systems," *IEEE Trans. Ind. Electron.*, vol. 58, no. 6, pp. 2274–2282, Jun. 2011.

[9] D. J. Thrimawithana and U. K. Madawala, "A three-phase bi-directional IPT system for contactless charging of electric vehicles," in *Proc. IEEE Int. Symp. Ind. Electron.*, Jun. 2011, pp. 1957–1962.

[10] J. Shin *et al.*, "Design and implementation of shaped magnetic-resonance-based wireless power transfer system for roadway-powered moving electric vehicles," *IEEE Trans. Ind. Electron.*, vol. 61, no. 3, pp. 1179–1192, Mar. 2014.

[11] M. Kim, H. Kim, D. Kim, Y. Jeong, H. Park, and S. Ahn, "A three-phase wireless-power-transfer system for online electric vehicles with reduction of leakage magnetic fields," *IEEE Trans. Microw. Theory Techn.*, vol. 63, no. 11, pp. 3806–3813, Nov. 2015.

[12] J. Lee, H. Shen, and H. Chang, "Design and implementation of contactless power track system with Y-shaped inductive pickup," *IET Power Electron.*, vol. 9, no. 3, pp. 536–545, 2016.

[13] U. Iruretagoyena, I. Villar, A. Garcia-Bediaga, L. Mir, and H. Camblong, "Design and characterization of a meander-type dynamic inductively coupled power transfer coil," *IEEE Trans. Ind. Appl.*, vol. 53, no. 4, pp. 3950–3959, Jul. 2017.

[14] S. Cui, Z. Wang, S. Han, and C. Zhu, "Analysis and design of multiphase receiver with reduction of output fluctuation for EV dynamic wireless charging system," *IEEE Trans. Power Electron.*, vol. 34, no. 5, pp. 4112–4124, May 2019.

[15] H. Li, Y. Liu, K. Zhou, Z. He, W. Li, and R. Mai, "Uniform power IPT system with three-phase transmitter and bipolar receiver for dynamic charging," *IEEE Trans. Power Electron.*, vol. 34, no. 3, pp. 2013–2017, Mar. 2019.

[16] H. Matsumoto, Y. Neba, K. Ishizaka, and R. Itoh, "Model for a three-phase contactless power transfer system," *IEEE Trans. Power Electron.*, vol. 26, no. 9, pp. 2676–2687, Sep. 2011.

[17] H. Matsumoto, Y. Neba, K. Ishizaka, and R. Itoh, "Comparison of characteristics on planar contactless power transfer systems," *IEEE Trans. Power Electron.*, vol. 27, no. 6, pp. 2980–2993, Jun. 2012.

[18] H. Matsumoto, Y. Shibako, Y. Shiihara, R. Nagata, and Y. Neba, "Three-phase lines to single-phase coil planar contactless power transformer," *IEEE Trans. Ind. Electron.*, vol. 65, no. 4, pp. 2904–2914, Apr. 2018.

[19] H. Matsumoto, Y. Neba, H. Iura, D. Tsutsumi, K. Ishizaka, and R. Itoh, "Trifoliate three-phase contactless power transformer in case of winding-alignment," *IEEE Trans. Ind. Electron.*, vol. 61, no. 1, pp. 53–62, Jan. 2014.

[20] H. Matsumoto, R. Nakashima, Y. Neba, and H. Asahara, "Proposal and verification of two-layer three-phase contactless power transformer," *IEEJ Trans. Ind. Appl.*, vol. 135, no. 5, pp. 539–547, 2015.

[21] S. Kim, G. A. Covic, and J. T. Boys, "Tripolar pad for inductive power transfer systems for EV charging," *IEEE Trans. Power Electron.*, vol. 32, no. 7, pp. 5045–5057, Jul. 2017.

[22] S. Kim, G. A. Covic, and J. T. Boys, "Comparison of tripolar and circular pads for IPT charging systems," *IEEE Trans. Power Electron.*, vol. 33, no. 7, pp. 6093–6103, Jul. 2018.

[23] Y. Shiihara *et al.*, "Three-phase contactless power transformer with magnet yoke," in *Proc. 19th Int. Conf. Elect. Mach. Syst.*, Nov. 2016, pp. 1–4.

[24] D. J. Thrimawithana, U. K. Madawala, A. Francis, and M. Neath, "Magnetic modeling of a high-power three phase bi-directional IPT system," in *Proc. 37th Annu. Conf. IEEE Ind. Electron. Soc.*, Nov. 2011, pp. 1414–1419.

[25] Y. Song, U. K. Madawala, T. Duleepa J, and A. P. Hu, "Cross coupling effects of poly-phase bi-directional inductive power transfer systems used for EV charging," in *Proc. IEEE 2nd Int. Future Energy Electron. Conf.*, Nov. 2015, pp. 1–7.

[26] Y. Song, U. K. Madawala, D. J. Thrimawithana, and A. P. Hu, "LCL and CL compensations for wireless three phase bi-directional EV charging systems," in *Proc. IEEE 2nd Annu. Southern Power Electron. Conf.*, Dec. 2016, pp. 1–6.

[27] C. Song *et al.*, "Three-phase magnetic field design for low EMI and EMF automated resonant wireless power transfer charger for UAV," in *Proc. IEEE Wireless Power Transfer Conf.*, May 2015, pp. 1–4.

[28] T. Kan, R. Mai, P. P. Mercier, and C. C. Mi, "Design and analysis of a three-phase wireless charging system for lightweight autonomous underwater vehicles," *IEEE Trans. Power Electron.*, vol. 33, no. 8, pp. 6622–6632, Aug. 2018.

[29] C. Song *et al.*, "EMI reduction methods in wireless power transfer system for drone electrical charger using tightly coupled three-phase resonant magnetic field," *IEEE Trans. Ind. Electron.*, vol. 65, no. 9, pp. 6839–6849, Sep. 2018.

[30] T. Kan, Y. Zhang, Z. Yan, P. P. Mercier, and C. C. Mi, "A rotation-resilient wireless charging system for lightweight autonomous underwater vehicles," *IEEE Trans. Veh. Technol.*, vol. 67, no. 8, pp. 6935–6942, Aug. 2018.

[31] A. Abdolkhani, A. P. Hu, G. A. Covic, and M. Moridnejad, "Through-hole contactless slipring system based on rotating magnetic field for rotary applications," *IEEE Trans. Ind. Appl.*, vol. 50, no. 6, pp. 3644–3655, Nov. 2014.

[32] A. Abdolkhani and A. P. Hu, "A contactless slipring system based on axially traveling magnetic field," *IEEE J. Emer. Sel. Topics Power Electron.*, vol. 3, no. 1, pp. 280–287, Mar. 2015.

[33] W. M. Ng, C. Zhang, D. Lin, and S. Y. R. Hui, "Two- and three-dimensional omnidirectional wireless power transfer," *IEEE Trans. Power Electron.*, vol. 29, no. 9, pp. 4470–4474, Sep. 2014.

[34] B. Lee, D. Ahn, and M. Ghovanloo, "Three-phase time-multiplexed planar power transmission to distributed implants," *IEEE J. Emer. Sel. Topics Power Electron.*, vol. 4, no. 1, pp. 263–272, Mar. 2016.

[35] D. Lin, C. Zhang, and S. Y. R. Hui, "Mathematical analysis of omnidirectional wireless power transfer—Part-I: Two-dimensional systems," *IEEE Trans. Power Electron.*, vol. 32, no. 1, pp. 625–633, Jan. 2017.

[36] D. Lin, C. Zhang, and S. Y. R. Hui, "Mathematic analysis of omnidirectional wireless power transfer—Part-II: Three-dimensional systems," *IEEE Trans. Power Electron.*, vol. 32, no. 1, pp. 613–624, Jan. 2017.

[37] E. S. Lee, J. S. Choi, H. S. Son, S. H. Han, and C. T. Rim, "Six degrees of freedom wide-range ubiquitous IPT for IoT by DQ magnetic field," *IEEE Trans. Power Electron.*, vol. 32, no. 11, pp. 8258–8276, Nov. 2017.

[38] B. H. Choi, E. S. Lee, Y. H. Sohn, G. C. Jang, and C. T. Rim, "Six degrees of freedom mobile inductive power transfer by crossed dipole Tx and Rx coils," *IEEE Trans. Power Electron.*, vol. 31, no. 4, pp. 3252–3272, Apr. 2016.

[39] A. Safaee, K. Woronowicz, and T. Dickson, "Reactive power compensation in three phase high output inductive power transfer," in *Proc. IEEE Elect. Power Energy Conf.*, Oct. 2015, pp. 375–380.

[40] A. Safaee, K. Woronowicz, and A. Maknouninejad, "Reactive power compensation scheme for an imbalanced three-phase series-compensated wireless power transfer system with a star-connected load," in *Proc. IEEE Transp. Electrific. Conf. Expo*, Jun. 2018, pp. 44–48.

[41] F. Zhang, *The Schur Complement and Its Applications* (Numerical Methods and Algorithms). New York, NY, USA: Springer, Mar. 2005.

[42] *Wireless Power Transfer for Light-Duty Plug-In/Electric Vehicles and Alignment Methodology*. Warrendale, PA, USA: SAE Int., Nov. 2017.

Jason Pries (M'10) received the B.S. degree in electrical engineering from the Milwaukee School of Engineering, Milwaukee, WI, USA, in 2009, and the M.S. and Ph.D. degrees in electrical engineering systems from the University of Michigan, Ann Arbor, MI, USA, in 2012 and 2015, respectively.

In 2015, he joined the Power Electronics and Electric Machinery Group, Oak Ridge National Laboratory, Oak Ridge, TN, USA, as a Research and Development Associate Staff Member. His research interests revolve around magnetics, including the design and optimization of electric machines and wireless charging pads, high-fidelity modeling of magnetic materials and systems, and high-performance computing for electromagnetic eddy current problems.

Dr. Pries is the recipient of a U.S. Department of Energy Vehicle Technology Office Distinguished Achievement Award and a UT-Battelle Research Accomplishment for his work on a nonrare earth electric motor. He is currently a Science Policy Fellow with the Society for Industrial and Applied Mathematics and an Associate Editor for the IEEE TRANSACTIONS ON INDUSTRY APPLICATIONS.

Veda Prakash Nagabhushana Galigekere (S'09–M'12–SM'19) was born in Bengaluru, India, in 1982. He received the B.E. degree in electrical engineering from Visvesvaraya Technological University, Bengaluru, India, in 2004, and the M.S. and Ph.D. degrees in electrical engineering from Wright State University, Dayton, OH, USA, in 2007 and 2012, respectively.

In 2008 and 2012, he was an Intern with the General Electric Global Research Center, Bengaluru, India. From 2012 to 2016, he was with the Lear Corporation, Southfield, MI, USA. He is currently a Research and Development Staff Member with the Power Electronics and Electric Machinery Group, Oak Ridge National Laboratory, Oak Ridge, TN, USA. His research interests include high-power wireless power transfer, high-frequency resonant converters, impedance source converters, and small-signal modeling and control of pulsewidth modulation dc–dc converters.

Dr. Galigekere was a Guest Associate Editor for the IEEE TRANSACTIONS ON POWER ELECTRONICS and is currently an Associate Editor for the IEEE TRANSACTIONS ON INDUSTRY APPLICATIONS.

Omer C. Onar (S'05–M'10–SM'18) received the Ph.D. degree in electrical engineering from the Illinois Institute of Technology, Chicago, IL, USA, in July 2010.

In July 2010, he received the Alvin M. Weinberg Fellowship at the U.S. Department of Energy's Oak Ridge National Laboratory, Oak Ridge, TN, USA, where he joined the Power Electronics and Electric Machinery Group. At Oak Ridge National Laboratory, he worked on advanced power electronics and electric drives, renewable energy, energy storage systems, and wireless power transfer systems.

Dr. Onar is the recipient of a U.S. Department of Energy Vehicle Technologies Office Distinguished Achievement Team Award and a UT-Battelle Research Accomplishment Team Award for his work on wireless power transfer systems in 2016. He is also the recipient of an R&D 100 Award jointly with Toyota TEMA for Wireless Charging of Electric Vehicles. He is an Associate Editor for the IEEE TRANSACTIONS ON TRANSPORTATION ELECTRIFICATION and the IEEE TRANSACTIONS ON POWER ELECTRONICS.

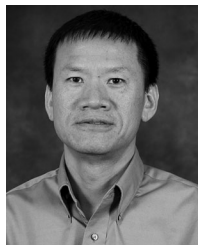

Gui-Jia Su (M'94–SM'01) received the B.S. degree in electrical engineering from the Wuhan University of Hydraulic and Electrical Engineering, Wuhan, China, in 1985, and the M.S. and Ph.D. degrees in electrical engineering from the Nagaoka University of Technology, Nagaoka, Japan, in 1989 and 1992, respectively, all in electrical engineering.

From 1992 to 1995, he was an Assistant Professor with the Nagaoka University of Technology. From 1995 to 1998, he was with Sanken Electrical Company, Ltd., Japan, where he was engaged in research and development of uninterruptible power supply, sensorless PM motor drive, and power factor correction for single- and three-phase rectifiers. In 1998, he joined the Power Electronics and Electric Machinery Research Center, Oak Ridge National Laboratory, Oak Ridge, TN, USA, as a Research Scientist, and is currently a distinguished member of the R&D staff. His research interests include dc–dc converters, inverters, wired and wireless battery chargers, and traction motor drives for electric vehicle applications.

Dr. Su is a Battelle Distinguished Inventor and a recipient of the US Department of Energy Vehicle Technologies Office Distinguished Achievement Award, 2019.